Marshall University

Marshall Digital Scholar

2019

Numerical simulation for the hydrodynamic performance of hydropower turbine near free surface

Zeda Yin

NUMERICAL SIMULATION FOR THE HYDRODYNAMIC PERFORMANCE OF HYDROPOWER TURBINE NEAR FREE SURFACE

A thesis submitted to
the Graduate College of
Marshall University
In partial fulfillment of
the requirements for the degree of
Master of Science
in
Mechanical Engineering
by
Zeda Yin
Approved by
Dr. Mehdi Esmaeilpour, Committee Chairperson
Dr. Yousef Sardahi
Dr. Xia Hua

Marshall University
December 2019

APPROVAL OF THESIS

We, the faculty supervising the work of Zeda Yin, affirm that the thesis, [*Numerical Simulation for the Hydrodynamic Performance of a Hydropower Turbine in Shallow Free Surface Flow*], meets the high academic standards for original scholarship and creative work established by the Master of Science in Mechanical Engineering and the College of Information Technology and Engineering. This work also conforms to the editorial standards of our discipline and the Graduate College of Marshall University. With our signatures, we approve the manuscript for publication.

Dr. Mehdi Esmaeilpour   Committee Chairperson   12/5/2019
                                                               Date

Dr. Yousef Sardahi   Committee Member   12/5/2019
                                                               Date

Dr. Xia Hua   Committee Member   12/5/2019
                                                               Date

ii

ACKNOWLEDGMENTS

First, I would like to use this opportunity to thank my advisor, Dr. Mehdi Esmaeilpour, for all his outstanding guidance, patience, and motivation in the preparation of this thesis. In the past two years, he has been a great source of knowledge and insight, and has always made himself available for any discussion and reviewing my work. Without his guidance and continued support, this thesis would not be possible.

I would also like to thank my committee members, Dr. Yousef Sardahi and Dr. Xia Hua, for taking time from their busy schedules to be on my committee and for reviewing my work.

Finally, I would like to thank my family and wife who have always supported me through the struggles of graduate school. Their love and support throughout this time have made the difference.

TABLE OF CONTENTS

LIST OF TABLES

LIST OF FIGURES

x

ABSTRACT

The performance of hydropower turbine in shallow water can be affected by the presence of free surface. Therefore, it is of great interest to investigate the influence of free surface on hydropower turbine performance through computational simulations. For a better understanding of flow field around hydropower turbine operating in shallow water, it is important to analyze the flow over a single hydrofoil beneath free surface first. Therefore, as the first part of this thesis, the Computational Fluid Dynamics (CFD) methodology was used for numerical simulation of 2D unsteady incompressible viscous flow over a hydrofoil under the free surface. The computation was based on finite volume discretization incorporated with the interface capturing volume of fluid method (VOF) to solve the flow field. The SST $k - \omega$ turbulence model was used to capture the turbulent flow in the field. A comparison of the present numerical results with experimental data and previous numerical results was presented to show how accurate to use turbulence model to simulate the result. A comprehensive simulation of quantities like wave profiles and forces was performed for various angles of attack ranging from -15 to 15 degree, and h/c from 0.2 to 0.9 resulting in low Froude numbers ranging from 0.1 to 0.9. It was found that the presence of the free surface reduced the lift coefficient by 33.24% in the case of Froude number of 0.3 and increased the drag coefficient by 79.01%. As the second part of this thesis, the numerical simulations of flow over a 3-blade vertical axis hydropower turbine were performed. A good agreement between the current simulations and previous works was observed through validation process. Then, a comprehensive simulation was performed for submerged depths ranging from h/R = 1.2 to 2, and tip speed ratio from λ = 1 to 3 in the case of fix-pitch blades. Variation in submerged depth brought substantial changes in the flow and vortex pattern. The results revealed that the presence of the free surface decreased the power coefficient by 19.05%

for the closest submerged depth of $h/R = 1.2$ at optimal tip speed ratio of $\lambda = 2.5$. The wave

breaking also occurred when the submerged depth was smaller than $h/R = 2$. In order to

understand the speeds limit for hydropower turbine, free-to-spin cases were investigated by six

DOFs method. The top speed had a 4.24% drop by comparing the largest and the smallest

submerged depths. Variable pitch improved the power coefficient by 28.10% when the free

surface was far from the hydropower turbine. However, the power coefficient improvement

became significantly small when the hydropower turbine was placed close to the free surface.

CHAPTER 1 INTRODUCTION

1.1. Hydropower energy

Due to rapid depletion of fossil fuels and increasing concentration of pollutants in the atmosphere during the past decades, the development of renewable energy based on environmentally friendly sources has recently started to attract interest of scientists and engineers to support the energy needs in a sustainable way. As it is shown in Figure 1, renewable energy provided about 11% of final energy consumption of the United States in 2018 and this is still increasing. Renewable energy usually comes from natural sources of energy that are clean, indigenous, and constantly replenished, such as wind, geothermal, solar and tidal energy. Among all the renewable energy sources, wind and solar energy significantly rely on the weather condition. However, hydroelectric energy from rivers and oceans is highly predictable which is the advantage of this energy source compared to other renewable sources and gives hydroelectric energy development an important potential for further electricity generation.
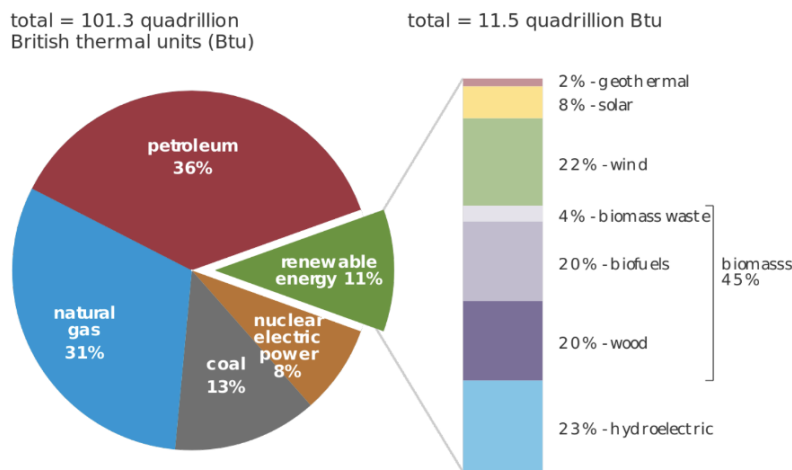
Figure 1. The annual energy consumption in the Unites States, 2018 (U.S. Energy Information Administration, Monthly Energy, April 2019).

The United States contains a large number of hydroelectric energy sources, especially in west coast, Hawaii, and Alaska, which can strongly supply the United States demand in electricity (Muljadi and Yu, 2015). Hydroelectric power can be created using both traditional hydroelectric plant-plants and marine energy technology. In hydroelectric plant-plants, settled water behind a dam flows down and rotates the turbines, which converts mechanical energy into electricity using generators. In marine energy technology, the kinetic and potential energy of ocean waves and river currents are used to run a mechanical part and produce electricity. Many types of technologies have been developed during last decade to use marine renewable energy to harvest electricity. Wave Energy Converter is one of these technologies in which wave energy of the oceans can be turned to electrical energy using the up-and-down motion of a floating device in the water. Wave Energy Converters are generally classified as Oscillating bodies, Oscillating Water Columns, and Overtopping devices (Day et al., 2015).
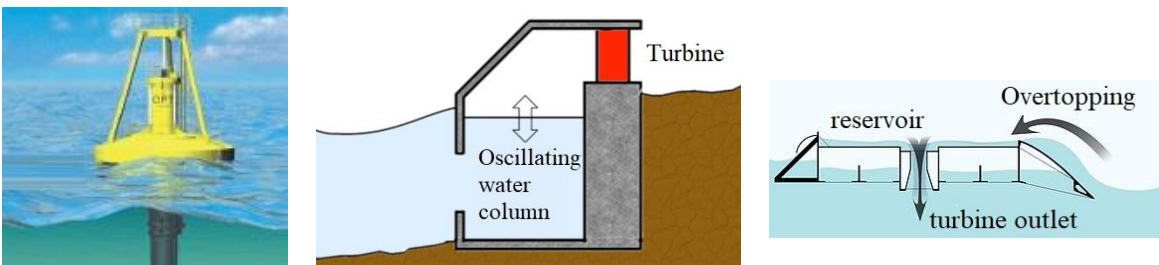
Figure 2.. Wave Energy Converters: (left) Oscillating bodies (middle) Oscillating Water Columns, and (right) Overtopping device.

Marine current (or hydropower) turbines are another technology in generating electrical energy from flowing flow of rivers and oceans. These types of turbines share highly similar characteristics with wind turbines both in device design and grid integration. The main difference between these two types of turbines is that the wind turbines operate in an unbounded flow field while hydropower turbines operate in bounded flow domain due to the presence of free surface and sea/river bed. The same as wind turbines, based on angle between turbine shaft axis and flow

direction, hydropower turbines are classified to horizontal-axis turbines (shaft axis aligned with the flow) and vertical-axis turbines (shaft axis normal to the flow). Examples of hydropower turbines are shown in Figure 3. The hydropower turbines can be either fully submerged or floated at specific distance from the free surface.
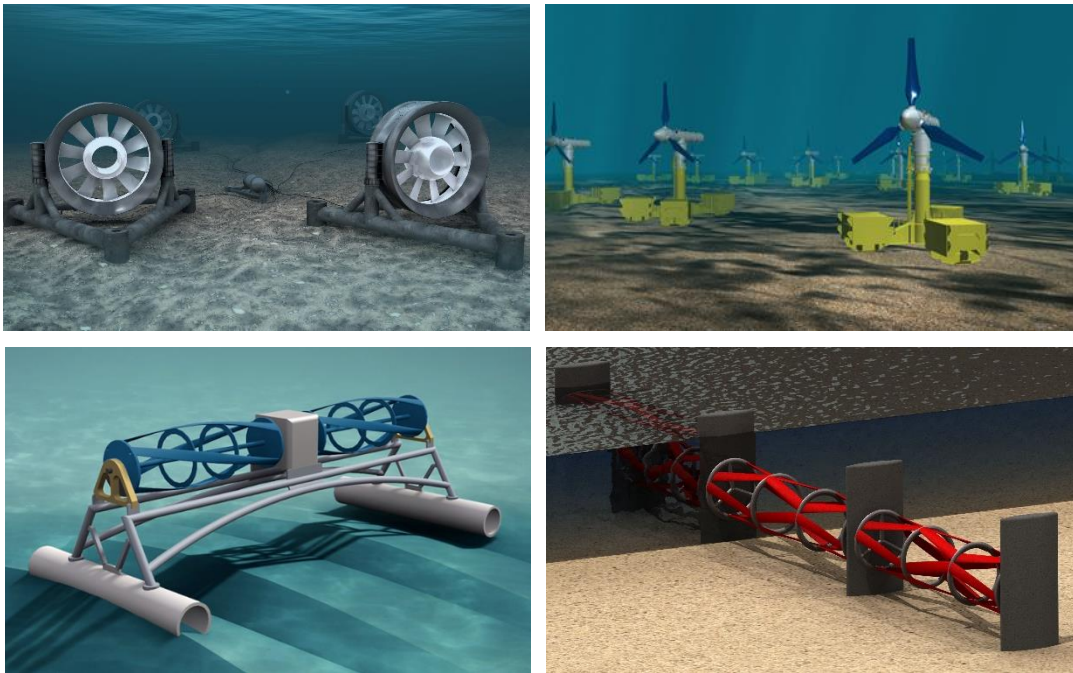
Figure 3. Example of horizontal axis (top) and vertical axis (bottom) hydropower turbines.

Studies show that wave energy and tidal energy are ranking as third and fourth largest resources of renewable energy in the world, following wind and solar energy (Chapman and Gross, 2001). In order to harvest energy from this massive number of environmental-friendly and renewable sources, many turbine designs have been proposed during last decades, and extensive analysis studies performed using both experimental tests and numerical simulations to improve the performance of Marine current turbines.

1.2. Background

1.2.1. State of turbine research

In 2019 Annual Energy Outlook, the U.S. Energy Information Administration Projects predict total power from turbines, both from wind power and hydropower, will increase to double size in 2040 (U.S. Energy Information Administration, 2016). Turbines have always been one of the most widely investigated and used energy harvest devices for centuries. Between 500 and 900 B.C., Persians used windmills to run pump water and grind grains, which is the most ancient model of wind turbine. Later, the use of windmills in food production spread from Persia to the surrounding areas in the Middle East. Finally, European countries such as The Netherlands started using windmills in draining lakes around 1,000 A.D. (Office of energy efficiency and renewable energy). The modern history researches for turbines can be traced to 1950s, and many researches and investigations of turbines have been conducted during the 1970s and 1980s oil crisis (Borg et al., 2014). Since 1970s, increase the efficiency including finding optimal tip speed ratio or optimal pitch angles has been the goal of most studies in turbine field. As it is mentioned earlier, since there is similarity in mechanical principles between wind turbine and hydropower turbine, reviewing the wind turbines could be a good start to have a better understanding of hydropower turbine's operating principle and the effects of different design parameters on its efficiency.

1.2.2. Vertical axis turbine vs. Horizontal axis turbine

Vertical axis turbine (VAWT) and Horizontal axis turbine (HAWT) are two common types of wind turbines that are commonly researched and used in both wind and marine field. Examples of these wind turbines are shown in Figure 4. The blade for vertical axis wind turbine

4

rotates perpendicularly to the ground and around the vertical axis, while horizontal axis turbine consists of blades that extracts wind energy on horizontal axis parallel to the ground.

Figure 4. The two main designs of wind turbines: vertical axis wind turbine (left), and horizontal axis turbine (right).

The advantages of vertical axis turbine have been proven in many aspects. For instance, vertical axis turbine has lower sound emission because it usually operates at lower tip speed ratio (Ferreira et al., 2007). Furthermore, vertical axis turbines are independence of wind direction. Different from the advantages of vertical axis turbine, the advantage of horizontal axis turbine is producing a higher power coefficient than similar size of VAWT because all blades are always involved in extracting energy from wind. Besides, HAWT are usually located at open ground and installed higher, which means wind speed can increase by 20% and the power output increase by 34% every ten meters up (Mertens, 2006). Since the advantages of horizontal axis turbine does not help in the water flow due to the bounded flow, vertical axis turbine could be a good research model of hydropower turbine that can operate in a shallow water flow with the influence of solid river/sea bed from bottom and deformable free surface on top of the turbine.

1.2.3. The performance of single hydrofoil

The vertical axis hydropower turbine can be used as a device to extract energy from river flow and ocean currents. The same as vertical axis wind turbine, this device consists of hydrofoil blades attached to a central shaft, which rotates around the turbine's axis. The performance of vertical axis hydropower turbine relies on lift force on hydrofoils. Therefore, in order to analyze and understand the performance of such a turbine, it is worth to study the performance of single hydrofoil under the free surface in the case of shallow water which the flow field is affected by the presence of deforming free surface.

The study of hydrofoil performance is always important in design of any turbine. Besides turbine's application, many other engineering applications such as ships and submarines also rely on hydrofoil study. When a hydrofoil is placed beneath the free surface, there is a fluid-structure interaction between free surface and the hydrofoil with complex near-field fluid flow. In flow over a hydrofoil close to free surface, at a certain velocity level, a wave breaking occurs which causes the fluctuations of both lift and drag forces. This phenomenon can heavily affect the performance and behavior of the hydrofoil motion. Thus, understanding hydrofoil-free surface is vital for designing any hydropower turbine, and it is important to simulate this interaction to predict the force on hydrofoil. The first part of this thesis, the simulation of flow over single hydrofoil is performed for various flow conditions and presented in Chapter 4. In the second part, a 3-blade vertical axis turbine is placed close to the free surface and the performance of the turbine is analyzed for various flow environments, and the simulations are presented in Chapter 5.

1.3. Literature Review

In this section, some significant highly related literatures have been reviewed. Some benchmark study reviews related to single hydrofoil operating closely under free surface will be presented in Section 1.3.1. Also, some previous works related to conventional hydrokinetic turbine will be presented in section 1.3.2.

1.3.1. Literature reviews on single hydrofoil

In early studies of hydrofoil submerged close to free surface, Parkin et al. (1956) presented a model test based on symmetric Joukowski section with 12% thickness to develop a qualitative theoretical expression for the pressure distribution. Hough and Moran (1969) also provided a theoretical method to develop a thin-foil approximation with linearized free surface boundary condition. The lift coefficients of two-dimensional hydrofoil were calculated versus submergence Froude number. The potential flow around a thin 2-D hydrofoil moving with constant velocity at a fixed depth beneath the free surface was simulated by Kennell and Plotkin (1984). It was assumed that the thickness-to-chord ratio of the hydrofoil and disturbances to the free stream were small. Froude number and depth of submergence were considered as two major variables to investigate the problem. Duncan (1981 and 1983) conducted experimental tests to investigate the wave breaking condition of this topic. An underwater towing system was used to drag a NACA0012 hydrofoil with various velocities of 0.6, 0.8, and 1.0 m/s. By observing and measuring the wave shape inclination of forward face, it was found that the total non-dimensional wave resistance is between 0.83 and 1; it is possible for either breaking or non-breaking. Sheridan et al. (1997) used experimental results to investigate the wave breaking effect, and they concluded that deflection of the jets increases if the gap ratio is reduced further to $h/d \leq 0.30$. It was also observed that external disturbances to the downstream region could

7

cause switching between states. Malavasi and Guadagnini (2007) conducted laboratory-scale experiments to study the interaction between a free-surface flow and a cylinder of rectangular cross-section. The authors concluded that the asymmetry of the flow condition strongly affects the lift coefficient; however, the influence on the drag coefficient is limited. In addition, the distortion of the free surface near the structure causes the dependency of the force coefficients on the Reynolds number.

Apart from the analytical and experimental studies, researchers have also conducted some numerical simulations. Hino et al. (1993) developed a self-made finite element method with unstructured grid to conduct hydrofoil NACA0012 under free surface flow simulation, with the focus on the accuracy of wave shape profile compared to experimental result. One advantage of this work was to predict the wave performance before creating the grid system. Reichl et al. (2005) investigated the fluid flow performance for flow passed over a cylinder close to free surface numerically. The $k - \varepsilon$ turbulence model was used to investigate free surface over cylinder cases with the gap ratio h/d ranging from 0.1 to 5.0, and Froude number from 0 to 0.7. The accuracy of the simulation was compared with experimental results from Sheridan et al. (1997). A variety of the wave shapes was provided and classified at maximum and minimum drag coefficient time. Xie and Vassalos (2007) developed a potential-based panel method to predict performance of 3D NACA4412 hydrofoil under free surface. A numerical solution was provided which was the combination of Rankine source distribution method and Dawson's double-body flow approach to predict the three-dimensional hydrofoil performance. They successfully verified their results with previous two-dimensional results, and provided comprehension results, including wave profile at central plane, pressure distribution at central plane, wave-making resistance, lift coefficient and force. Karim et al. (2014) simulated flow

8

passed over NACA0015 hydrofoil to prove the feasibility of using two dimensional CFD method

to simulate the problem. Four cases of submergence depths, h/c, ranging from 0.91 to 4, were

investigated, and velocity and pressure contours were presented for computational domain. The

numerical simulations using OpenFOAM were carried out by Prasad et al. (2015) to extend

Karim et al. (2014) work by adapting standard $k - \varepsilon$ turbulence model to investigate six more

submergence depth cases for NACA0012 hydrofoil. It is observed that the non-breaking wave

profile was compatible with experiment result even profile was slightly under-estimated. The

drag and lift coefficient parameters in their numerical simulation agreed well with some

published previous experimental results. This work is another proof of feasibility of using two-

dimensional CFD method for flow past hydrofoil near the free surface topic.

1.3.2. Literature reviews on hydropower turbine

Conventional hydrokinetic turbine topics have been researched for a long time. The

investigation of wave energy harvest can be traced to Budal and Falnes (1975) and Evans (1976).

Hwang et al. (2009) carried out a two-dimensional CFD simulation and conducted experiments

verified optimization of conventional longitudinal cycloidal water turbine by the strategy of

variable pitches. They used a sinusoidal type of variable pitch angles to improve the approximate

25% turbine performance compared to their fixed pitch results. Wang et al. (2012) provided a

novel design of composite horizontal water turbine and adapts three-dimensional CFD

simulation to test its performance. It was found that adapting nozzle and diffuser could increase

the pressure drop and extract more power from available flow energy. Day et al. (2015) provides

a comprehensive review of marine renewable energy devices. They stated that there is a general

lack of availability of full-scale or large-scale data from wave energy generation with physical

testing and numerical modeling, and they wanted more researchers to get involved in wave

energy generation investigations. Sangal et al. (2016) used CFD based Analysis to test a Kaplan type of Hydraulic turbine and provided a detailed solution with power harvest and power loss. They concluded that Kaplan blade tips and regions around trailing edges were more vulnerable after the analysis of silt behavior. Kaniecki & Krzemianowski (2016) adapted CFD method to analyze the high-speed Francis turbines with 1200 to 1280 rpm and provided a curve of energy harvested. Teran et al. (2016) implemented Artificial Neural Networks and optimizations based on Genetic Algorithms to optimize a 500-KW Francis turbine performance and verified the results by CFD simulation. They found that the highest point efficiency has an improvement of 14.77% after their optimization. They also verified some other factors such as static strength, fatigue and resonance.

Aparna and Ramadan (2017) performed a three-dimensional CFD analysis of horizontal turbine blades to harvest tidal energy. They analyzed fluid flow over the turbine blades by varying the pitch angles for low tidal condition and high tidal condition, and they found a higher pitch angle was suitable for low tidal condition. Babarit (2017) provided a comprehensive book to guide wave energy investigation. He used airy regular mathematical model to simulate two-dimensional wave condition, analyzed the advantages of current commonly used devices, and provided overall guide direction for a variety of wave energy convector to capture the wave energy. Ohm and Tetursson (2017) used OpenFOAM with SST $k - \omega$ turbulent model to test the small hydro turbine performance improvement after their optimization. The authors found 4.4% higher efficiency and 72% lower pressure drop. A three-dimensional CFD analysis of the energy conversion process in a fixed oscillating water column device with a Wells turbine was conducted by Filianoti et al. (2018). A fixed oscillating water column device was used to create an oscillating wave input to test section. The free surface condition in both analytical and

numerical methods was predicted and described. Ikoma et al. (2018) conducted experimental study of NACA-0018 based H-type Darrieus vertical hydropower turbine towed by a marine vehicle. The power coefficients of turbine were studied by varying different pitch angle (maximum 30-degree) and flow velocity input (up to 1.5 m/s), and the power coefficients ranged from 0 to 0.2 were obtained. Siegel (2019) came up with an innovative design of lift-based cycloidal wave energy converter, which was similar to transverse H-type Darrieus turbine, to harvest wave energy. He also presented a numerical approach to compute the mean annual power. Bubbar (2018) proposed a design for a turbine placed at the position very close to free surface, to capture the wave energy and used both analytical and numerical method to analyze the performance. Suzuki et al. (2019) performed a numerical simulation with actuator disk method to conduct a study on prediction of hydropower turbine operating in open channels condition. Different from other hydro turbine study, they concentrated on free surface level change rather than hydro turbine performance.

1.4. Motivations and Objectives

1.4.1. Motivations

The world has significant marine renewable energy resources. This kind of energy plays a fundamental role in reducing greenhouse gas emissions caused by burning traditional fossil fuels. To make less severe effects of climate change on the planet earth, it is vital to develop new technology to extract energy from renewable resources. Currently, only wind turbines have assured level of development. However, there are still other technologies that have not reached yet the same level of technological maturity and economic interest as wind turbines in extracting energy from renewable energy resources such as oceans and revisers. With plenty of water

11

resources all around the world, the hydropower technology could be able to provide renewable and clean energy to the entire world.

1.4.2. Objectives

Among more than hundreds of researches, the performance of vertical-axis hydropower turbine in presence of free surface has not been investigated. For a better understanding of flow field around hydropower turbine operating in shallow water, it is important to analyze the flow over a single hydrofoil beneath free surface. The understanding of the free surface effect and its interaction with near-surface hydrofoil has not yet been studied. Therefore, one of the objectives in this thesis is to use computational fluid dynamics (CFD) method to investigate the hydrodynamic forces on the hydrofoil and the change of nearfield flow. Submerged depth and angle of attacks will be two main variables in analyzing fluid flow over single hydrofoil. The lift and drag coefficients as two important parameters in performance of hydrofoil and fluid flow as a function of submerged depth will be investigated.

The other motivation of this thesis is to provide a comprehensive investigation of hydropower turbine performance when it is placed close to free surface, which has never been conducted before. Due to the presence of free surface, turbine may lose some energy to create an unsteady wave in the downstream. Understanding how much energy will lose to create unsteady wave in the downstream is another important objective, which will be investigated using computational fluid dynamics (CFD) method. The numerical results will be presented corresponding to different submerged depths and tip speed ratios (TSR). Lastly, Variable pitch method as one of the most common used optimizations for turbine will also be studied to find whether or not this method is still useful to improve the performance of hydropower turbines.

1.5. Thesis structure

The body of this thesis consists of six chapters, in which performance of single hydrofoil and whole hydropower operating in shallow water close to the free surface are studied. These chapters can be read separately. Chapter 2 includes mathematical models and numerical methods to solve the Navier-Stokes equations required for flow field. The equations governing the flow, turbulence modeling, and discretization methods are presented in detail with their specific simplifications. In Chapter 3, the validation studies are performed for both single hydrofoil and hydropower turbine cases. In the case of single hydrofoil, the validation cases are (i) a numerical simulation of flow over stationary cylinder below the free surface (Reichl et al., 2005); and (ii) an experimental analysis of flow over a stationary hydrofoil under free surface (Duncan, 1981 and 1983). In the case of hydropower turbine, the validation cases are (i) a numerical simulation on performance of 3- bladed VAWT (Subramanian et al., 2017) in which the turbine rotates with specific angular velocity to make the tip speed ratio (TSR) to a certain fixed value; and (ii) an experimental analysis of flow over a turbine in which the turbine is left free to rotate (Rainbird, 2016; Hill et al., 2009; Bianchini et al., 2011; Chua, 2002). Chapter 4 provides the problem of the two-dimensional structure of the flow around single hydrofoil near the free surface. The computations are performed for various flow conditions. This chapter is self-contained and divided into subsections with problem statement, and simulation design along with results and discussion, and conclusions. The problem of vertical axis hydropower operating in shallow water is presented in Chapter 5. Numerical simulations are performed to investigate the fluid-structure interactions between the free surface and turbine under different operating conditions. Finally, Chapter 6 summarizes conclusions and recommendations for future work.

CHAPTER 2 NUMERICAL METHODOLOGY

In this chapter, the governing equations of the finite volume method, volume of fluid, turbulence modeling and six DOFs are presented. The incompressible Reynolds Averaged Navier-Stokes (RANS) equations are employed to solve flow domain in this work. The volume of fluid (VOF) multiphase flow modeling method is utilized to simulate the air-water interface of free surface, and the $k - \omega$ SST model is employed as turbulence model in this thesis.

2.1. Governing equations

The RANS equations in a Cartesian tensor notation can be expressed as conservative of mass equation, *x*-direction momentum equation, and *y* direction momentum equation. For an isothermal system with no mass transfer and no phase change, the conservation equations are considered as:

$$\frac{\partial(\rho)}{\partial t} + \frac{\partial(\rho u_i)}{\partial x_i} = 0, \tag{2.1}$$

$$\frac{\partial(\rho u_i)}{\partial t} + \frac{\partial(\rho u_i u_j)}{\partial x_i} = -\frac{\partial p}{\partial x_i} + \frac{\partial}{\partial x_{ij}}\left[\mu\left(\frac{\partial u_i}{\partial x_j} + \frac{\partial u_j}{\partial x_j}\right) - \rho\overline{u_i'u_j'}\right] + \rho g_i + S_m, \tag{2.2}$$

where the body force due to gravity g is decomposed into components g_i, for the y-direction, and the term S_m stands for the source term. Also, u is the mean velocity, and *i* and *j* are equal to 1 or 2, representing the two directions in the Cartesian coordinate system. The term $\rho\overline{u_i'u_j'}$ in Eq. (2.2) is called the Reynolds stresses and can be estimated by means of closing equations such as the Reynolds stress model (RSM). Using the Boussinesq assumption, a linear dependence on eddy viscosity μ_t and the turbulence kinetic energy k is first written as:

$$\rho\overline{u_i'u_j'} = 2\mu_t\left(\frac{\partial u_i}{\partial x_j} + \frac{\partial u_j}{\partial x_i}\right) - \frac{2}{3}\rho k\delta_{ij}, \tag{2.3}$$

where μ_t is the turbulent eddy viscosity and δ_{ij} is the Kronecker delta, which takes on a value of 1 if i=j and 0 otherwise.

2.2. Volume of Fluid (VOF)

The volume of fluid (VOF) method, a Euler-Euler framework appropriate for free surface flow, is a surface tracking technique which is designed for two or more immiscible fluids when the position of the interface between the fluids is of interest. This model was introduced by Hirt and Nichols (1981). This method treats all existing phases in flow field as continuous phase, without allowing the phases to be interpenetrating. In theory, a phase indicator function with a value between zero and one is used to track the interface between phases of multiphase flow. In the case of two-phase flow, the transport equations are solved for mixture properties such as density and viscosity. Also, an advection equation for the indicator function is solved to track the interface between two phases. Since there is a free surface in all simulations, the volume of fluid (VOF) multiphase flow modeling method is applied to simulate the air-water interface. The interface between the air as primary fluid and the water as secondary fluid is tracked by solving the conservation equation for the volume fraction of each phases as:

$$\frac{1}{\rho_q}\left[\frac{\partial(\rho_q \alpha_q)}{\partial t} + \frac{\partial(\rho_q \alpha_q u_i)}{\partial x_i} = S_{\alpha_q} + \sum_{p=1}^{n} \dot{m}_{pq} - \dot{m}_{qp}\right] \tag{2.4}$$

where the phase volume fraction (α) has a value of 0 or 1 when a control volume is entirely filled with air or water, and a value between 0 and 1 if an interface is present in the control volume. In Eq. (2.4), ρ_q represents the density of the qth fluid, S_{α_q} represents a mass source term, $\dot{m}_{pq}$ and $\dot{m}_{qp}$ are the mass transfer from fluid q to p and mass transfer from fluid p to q, respectively (ANSYS FLUENT User Guide Release 19.1, 2018).

In the case of open channel flow, there is no mass source and mass transfer between fluids, and the flow is incompressible. Therefore, Eq. (2.4) can be simplified to:

$$\frac{\partial(\rho_q \alpha_q)}{\partial t} + \frac{\partial(\rho_q \alpha_q u_i)}{\partial x_i} = 0 \qquad (2.5)$$

Considering ideal mixtures, the mixture has a volume equal to the sum of the volumes of the individual components, the calculation of the mixture density and viscosity of the air-water mixture in each cell is:

$$\rho = \alpha_a \rho_a + \alpha_w \rho_w \qquad (2.6)$$

$$\mu = \alpha_a \mu_a + \alpha_w \mu_w \qquad (2.7)$$

where ρ_a, ρ_w are the densities of air and water, respectively, and α is volume fraction which represents the mass percentage in one volume. The interfacial forces acting on phases is the connection between the momentum equations of different phases. These interfacial forces are unknown and needed to be modeled.

2.3. Turbulence modeling

The choice of turbulence model is a key parameter in simulation of turbulent two-phase flow. Choosing a good turbulent model is complicated for complex flow structure such as flow over wind or hydropower turbine. In this thesis, the two-equation Shear-Stress Transport (SST) $k - \omega$ model (Menter, 1993 and 1994) is used to estimate the Reynolds stresses $\rho \overline{u_i' u_j'}$. The SST $k - \omega$ turbulence model is a RANS-based approach that has its origins associated with the Boussinesq eddy-viscosity approximation. According to Boussinesq approximation, the momentum flux due to random molecular fluctuations is comparable to those created by random turbulent fluctuations. The SST $k - \omega$ model has a similar form to the standard $k - \omega$ model. This model is a blending of two of the more popular turbulence models used in external flow applications, the $k - \omega$ model (Wilcox, 1993) superior in near-wall regions, and the $k - \varepsilon$

16

model, which performs better outside boundary layers, particularly in applications involving flow separation. Switching from $k - \omega$ model to $k - \varepsilon$ model occurs via a blending function. Due to the advantages of SST $k - \omega$ model, this model has been used in various RANS-based CFD simulations in both hydrodynamics and aerodynamics.

The SST $k - \omega$ model requires two additional transport equations to calculate the eddy viscosity; one for the turbulence kinetic energy k and one for the turbulence dissipation rate ω:

$$\frac{\partial(\rho k)}{\partial t} + \frac{\partial(\rho \bar{u}_i k)}{\partial x_i} = \frac{\partial}{\partial x_i}\left[\Gamma_k \frac{\partial k}{\partial x_i}\right] + G_k - Y_k + S_k, \tag{2.8}$$

$$\frac{\partial(\rho \omega)}{\partial t} + \frac{\partial(\rho \bar{u}_i \omega)}{\partial x_i} = \frac{\partial}{\partial x_i}\left[\Gamma_\omega \frac{\partial \omega}{\partial x_i}\right] + G_\omega - Y_\omega + D_\omega + S_\omega \tag{2.9}$$

where Y_k and Y_ω are the dissipation of k and ω due to turbulence, G_k is the generation of turbulence kinetic energy due to the mean velocity gradients, G_ω is the generation of ω, D_ω is the cross diffusion term, and S_k and S_ω are source terms. Γ_k and Γ_ω are the effective diffusivities of k and ω, and are calculated using the following equations:

$$\Gamma_k = \left(\mu + \frac{\mu_t}{\sigma_k}\right) \tag{2.10}$$

$$\Gamma_\omega = \left(\mu + \frac{\mu_t}{\sigma_\omega}\right) \tag{2.11}$$

where μ_t is the turbulent viscosity, σ_k and σ_ω are the turbulent Prandle numbers for k and ω, respectively. The intrinsic of the $k - \omega$ SST is explained in detail in (Wilcox, 1993), for instance the calculation of S and handling of blending functions (e.g., F_1) as well model constants ($\alpha, \beta, \beta^*, \sigma_k$ and σ_ω), some of which are themselves blended based on dimensionless wall distance. The cross-diffusion term, D_ω, is defined as (Menter, 1993 and 1994):

$$D_\omega = \frac{2\rho \sigma_{\omega 2}}{\omega} (1 - F_1) (\nabla k . \nabla \omega) \tag{2.12}$$

where $\sigma_{\omega 2}$ is a model coefficient and F_1 represents the blending function which is defined as:

$$F_1 = \tanh\left(\left[min\left(max\left(\frac{\sqrt{k}}{0.09\omega d}, \frac{500\nu}{d^2\omega}\right), \frac{2k}{d^2 CD_{k\omega}}\right)\right]^4\right)$$

(2.13)

where $CD_{k\omega}$ is a cross-diffusion coefficient and d is the distance to the wall. The shear stress transport blending function, F_2, is also defined as:

$$F_2 = \tanh\left(\left(max\left(\frac{\sqrt{k}}{\beta^*\omega d}, \frac{500\nu}{d^2\omega}\right)\right)^2\right)$$

(2.14)

where β^* is a model coefficient. The handling of blending functions and model constants can be readily found in Menter et al. (2003).

2.4. Sliding Mesh

For a flow problem such as the wind or hydropower turbine with moving boundaries, a mesh updating method is required to maintain a valid mesh while the flow domain geometry changes. The relative motion of rotating and stationary components of the turbine will give rise to unsteady interactions. Since boundary of rotating component is parallel to the boundary of stationary component, instead of using dynamic mesh method, a technique so called sliding mesh can be a good choice in order to simulate the flow field. The sliding mesh technique is a particular case of dynamic mesh technique wherein only the boundary between two zones gets updated in time while the different mesh zones are considered as rigid zone. Therefore, there will be a relative motion along the interface boundary in discrete steps during the calculation. This interface is updated every time step as well. An illustration of sliding mesh technique is shown in Figure 5.
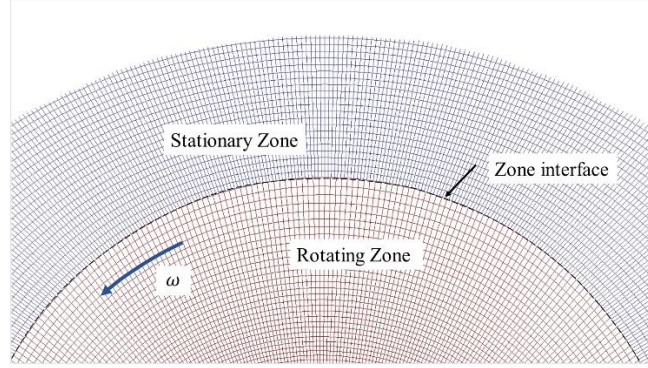
Figure 5. The concept of sliding mesh technique using in flow over rotating turbine.

2.5. Six DOFs

In most of works related to the simulation of turbines, the tip speed ratio is given, and the rotor will rotate in a constant angular velocity. However, the angular velocity of the rotor is not specified in an unsteady flow-driven turbine simulation. In the case of flow-driven turbine simulation, the turbine rotates around its axis at a certain rotational speed by balancing the moment of inertia, the hydrodynamic moment, and the imposed counter moment on the turbine. The rotational motion of the turbine can be calculated as (Le et al., 2014):

$$I\theta = M_F - M_A \qquad (2.15)$$

where I represents the moment of inertia of the turbine, M_F and M_{FA} are the total hydrodynamic moment on the turbine blade and applied moment on the rotational axis for finding the turbine's power, respectively. Therefore, the angular velocity of the turbine can be obtained as (Le et al., 2014):

$$\omega = \int \frac{(M_F - M_A)}{I} dt \qquad (2.16)$$

The hydrodynamic moment can be calculated using six DOFs solver in FLUENT by integrating pressure and shear stress on the surface of the blade to estimate the motion of a rigid object. Therefore, the moment of inertia of the blade and the constraint of the turbine motion in the x, y, and z directions are required which can be included in simulation using the UDF file.

CHAPTER 3 VALIDATION AND INDEPENDENCE STUDY

In this chapter, extensive validation works are performed to prove the accuracy and liability of the numerical set-up in simulation of flow field over single hydrofoil and hydropower turbine. The grid independency is also performed to ensure that the results in this study are independent of the mesh quality. Finally, since all simulations are unsteady computation, finding a proper time step can significantly affect the cost and accuracy of simulation. Therefore, the time step independency is also evaluated for both single hydrofoil and hydropower turbine.

3.1. Validation for single hydrofoil

To make sure that the flow over the hydrofoil beneath a free surface is accurately simulated, two sets of validation studies including the experimental and numerical studies are performed where the geometrical and operational characteristics are selected to be the same or similar to those in this study. The validation cases are (i) a numerical simulation of flow over stationary cylinder below the free surface (Reichl et al., 2005) and (ii) an experimental analysis of flow over a stationary hydrofoil under free surface (Duncan, 1981 and 1983). The operational and geometrical characteristics for each case are explained in this section.

3.1.1. Flow over hydrofoil

Duncan (1981 and 1983) used experimental method with submerged depth around $h = 0.9c$ to investigate the wave breaking condition. A solid aluminum hydrofoil with a NACA0012 shape was towed inside a tank that was 61cm deep. The hydrofoil had a chord of 20.3cm and its maximum thickness was 2.54cm at 6.1cm from the nose. Based on the problem setup, due to the presence of free surface flow, the dimensionless parameters are the Reynolds number and Froude number which are respectively defined as:

$$Re = \frac{\rho_w U_w c}{\mu_w} \tag{3.1}$$

$$Fr = \frac{U_w}{\sqrt{gc}} \tag{3.2}$$

where ρ_w is the density of water, g is the acceleration due to gravity, and μ_w is dynamic viscosity of water. By placing the hydrofoil at the depth of $h/c = 0.91$ and $\alpha = +5°$, it was towed in the speed of $0.8 m/s$ resulting in Froude number $Fr = 0.57$ and Reynolds number $Re = 1.59 \times 10^5$. By simulation of the hydrofoil in the same conditions as the experiment reported by Duncan (1983), the wave elevation on the free surface was compared with the experimental data, as shown in Figure 6. The comparison shows a very good agreement between the present CFD result and the experimental data. The reason why simulation result is slightly deviated from experimental result, especially in the second downstream wave, is that the SST $k - \omega$ model may produce a bit too large turbulence levels in regions with large normal strain, like stagnation regions and regions with strong acceleration, but the accuracy of numerical simulation is still in a very good condition. Comparing the current CFD with those from Karim et al. (2014) reveals that the current study provides a better prediction of the wave elevation than the numerical study by Karim et al. (2014) with slightly higher deviation from the experimental result for the same condition.
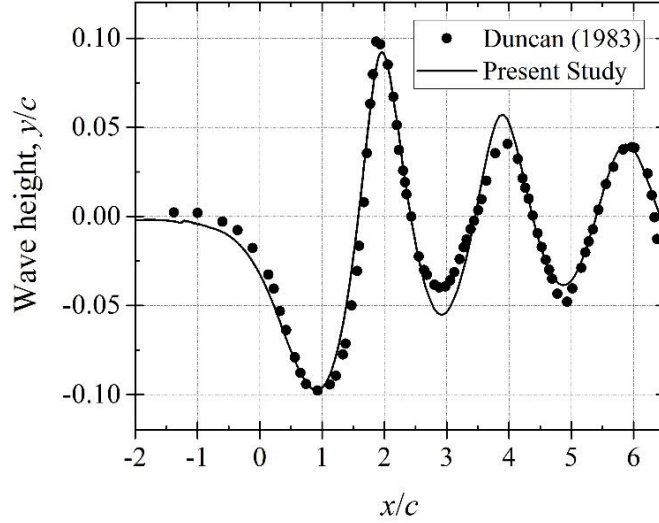
Figure 6. The wave elevations for NACA0012 hydrofoil at $h/c = 0.91$ and $Fr = 0.57$ compared against experiment results by Duncan (1983).

3.1.2. Flow over cylinder

The second validation is performed for flow over a cylinder and compared with numerical results presented by Reichl et al. (2005), which describe the situation of a jet attached to the cylinder in a short period of time when the gap ratio is less than 0.3 at Froude number between 0.3 and 0.6. The diameter of cylinder is d, and the distance between free surface and top of cylinder is h. The gap ratio is h/d, which is an important parameter and variable investigated in this validation. The upstream velocity inlet is u, and the acceleration of gravity is g. For the geometry set up, the center of cylinder is located at the origin of 2D Cartesian coordinate system. The distance from cylinder center to upstream inlet boundary is $15d$ in order to simulate a good quality of inlet. The distance to top and bottom boundary is $20d$. The distance to the outlet is $30d$ in order to simulate the complete results for vertex, wave, and jets. The computational mesh system is shown in Figure 7. The simulation is based on VOF (Volume of Fluid) method is adapted to capture the free surface between air and water.
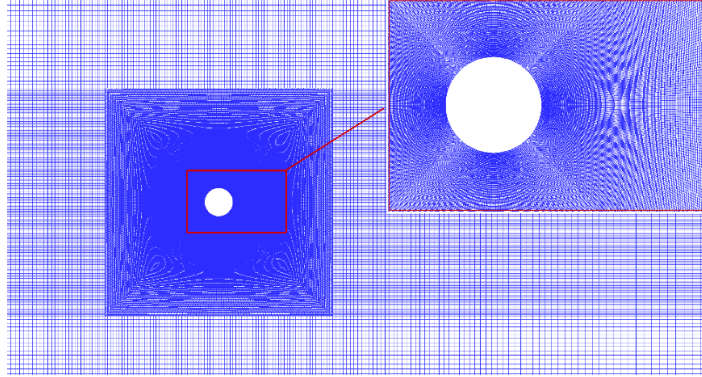
Figure 7. The grid system in entire domain and a close-up view of the grid near the cylinder for validation.
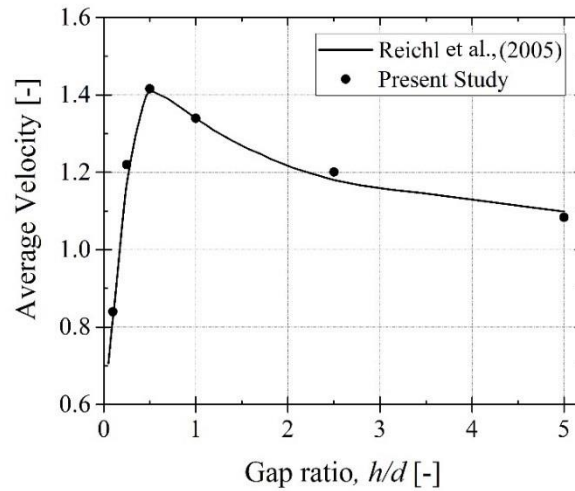
Figure 8. Comparison of average velocity direct above the cylinder as a function of gap ratio at the point of maximum lift against the results from Reichl et al. (2005).

Figure 8 and Figure 9 show the comparison between present CFD results and numerical results presented by Reichl et al. (2005) for Froude number of $Fr = u/\sqrt{gd} = 0.3$ and the submerged depth (h/d) varying from 0.2 to 5. As it is shown in Figure 8, at the intermediate gap ratio, approximately between 0.5 and 0.6, the average velocity above the cylinder comes to the peak value. The peak value is approximately equal to 1.42, which is close to the result of Reichl et al. (2005). As the gap ratio becomes smaller or larger than that intermediate gap ratio value,

23

the average velocity curves become smaller as expected which is in good agreement with

computed average velocities directly above the cylinder reported by Reichl et al. (2005).

Figure 9 compares the local Froude number (Fr_L) as function of gap ratio against the

results from Reichl et al. (2005). The Froude number is defined based on maximum velocity in

the region directly above the cylinder. As it is expected, higher h/d results in lower maximum

velocity above the cylinder with smaller Fr_L. This behavior can be seen in Figure 9, which is in

good agreement with the same results from Reichl et al. (2005).
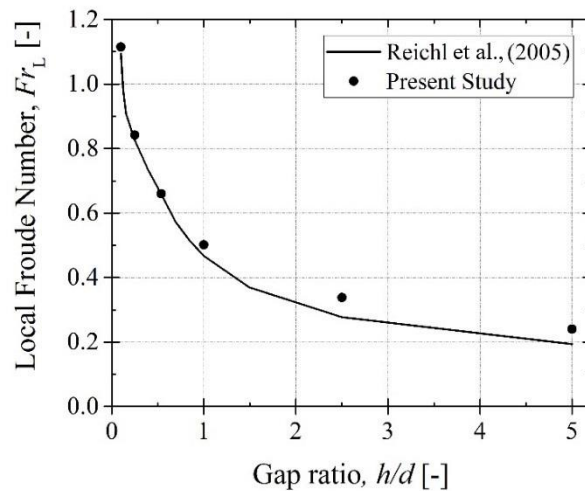
Figure 9. Comparison of local Froude number (Fr_L) as function of gap ratio (the Froude number based on maximum velocity in the region directly above the cylinder) against the results from Reichl et al. (2005).

The process of jet formation at different times of 0.5s, 0.7s, 1.1s, and 2.1s in Figure 10.

When the gap ratio is smaller than 0.3, the wave breaking will produce the bubbles in the water.

This figure is made in order to understand how the jets come out.
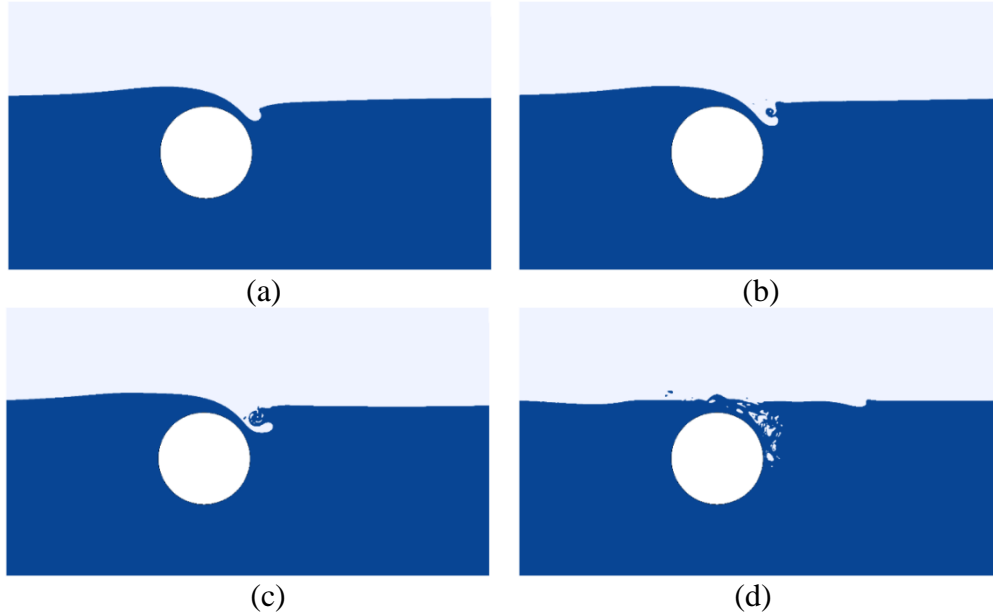
Figure 10. Jet formation over the cylinder for case of $h/d = 0.1$ and $Fr_L = 0.3$ at time of (a) 0.5s, (b) 0.7s, (c) 1.1s, and (d) 2.1s.

3.2. Grid Independency for single hydrofoil

Grid independence test is extremely important prior to extensive numerical simulations. To check the grid independency of the results, three grid systems namely coarse mesh, medium mesh and fine mesh are considered for the hydrofoil at angle of attack of $\alpha = +5°$. The coarse mesh consists of 342,250 cells, the medium one with 537,070 cells, and the fine mesh with 664,080 cells. The time history of lift coefficient and the average lift coefficient using these three meshes are shown in Figure 11 and Figure 12, respectively. According to these figures, there is almost no change in results for increasing total number of cells from medium to fine grid system. Maybe more refined mesh could produce better results but for the limitation of computer resources, the medium grid system is chosen for present study to save the computational time.
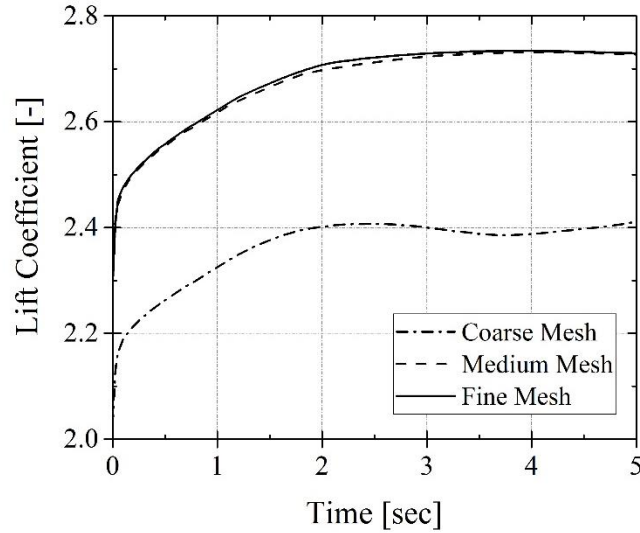
Figure 11. The time history of lift coefficient for three different grid systems.
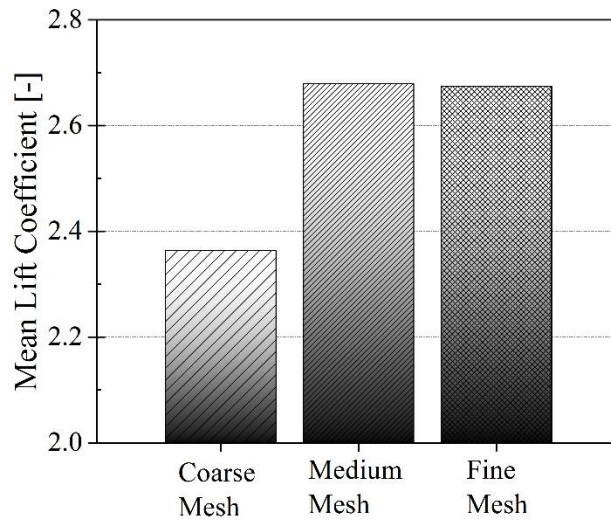
Figure 12. The average lift coefficient for three different grid systems.

3.3. Validation for hydropower turbine

To make sure that the hydrodynamic performance of the turbine under the free surface is accurately simulated, it is required to assess the validity of the proposed numerical modeling. Even though the purpose of this paper is to investigate the hydropower turbine performance in shallow water, the researches and investigations about hydropower turbine are still very limited compared to wind turbine. Due to the similarity between the simulation of Vertical Axis Wind Turbine (VAWT) and vertical 3-blade hydropower turbine, the reliability of the proposed

26

approach in calculating the performance of the turbine can be achieved by applying the numerical settings to the simulation of the VAWT. The simulation of VAWT is based on two approaches; rotating turbine with a certain angular velocity, and rotating turbine based on the torque experienced over time with activated six DOFs. Two sets of validation including the numerical and experimental studies are performed where the geometrical and operational characteristics are similar to those in this current work. The validation cases are (i) a numerical simulation on performance of 3- bladed VAWT (Subramanian et al., 2017) in which the turbine rotates with specific angular velocity to make the tip speed ratio (TSR) to a certain fixed value; and (ii) an experimental analysis of flow over a turbine in which the turbine is left free to rotate (Rainbird, 2016; Hill et al., 2009; Bianchini et al., 2011; Chua, 2002). The operational and geometrical characteristics for each case are explained in this section.

3.3.1 Validation with specific angular velocity approach

In the first validation study, a certain load is added to a wind turbine and it operates in a certain fixed tip speed ratio (TSR). The purpose of this validation is to verify the accuracy of moment coefficient with angular position and power coefficient with tip speed ratio. The turbine size and blade profile are the same as the one in Subramanian et al. (2017). The computational parameters of this case are given in Table 1.

Table 1. Main features of the rotor by Subramanian et al. (2017).

Parameter	
Airfoil profile	NACA0015
Chord Length, c [m]	0.42
Rotor Diameter, D [m]	2.7
Freestream velocity, U_∞ [m/s]	10
Reynolds numbers based on rotor radius [-]	9.24×10^6
Reynolds numbers based on chord length [-]	2.89×10^6
Number of Blades [-]	2, 3

The inlet velocity is 10 m/s, and turbulent intensity of 1% and viscosity ratio of 10 are selected for this case. Pressure outlet on the right side of the computational domain is set as zero relative pressure to simulate as an open condition. Both top and bottom side of the computational domain are set as symmetry. The interface between rotating inner domain and stationary outer domain is connected by sliding mesh technique. Angular velocities that calculated from tip speed ratio (TSR) are added on the cell zone conditions. The case is initialized by standard initialization, and all initialization data are absolute value from inlet. Figure 13 shows a comparison between the numerical predictions of the moment coefficient, in 2-blade and 3-blade cases in tip speed ratio of 2.5, and the corresponding numerical data obtained by Subramanian et al. (2017). As it is shown in this figure, for 2-blade case, the maximum moment coefficient occurs at near 180° position from start-up position, and two blades have the identical moment coefficient curve. For 3-blade case, the maximum moment coefficient happened at near 90° position from start-up position, and three blades have the identical moment coefficient curve as well. Furthermore, the results indicate that the blade generates energy by passing through upwind region, and it generates the maximum energy when it is perpendicular to the upwind. At downwind region, blade cannot generate any energy, and it needs energy from other blades to spin. This comparison shows a good agreement between the CFD prediction and the experimental data, which confirms that the numerical setup and the mesh are convincing in the numerical study of the motion of the VAWT. The good agreement between the CFD prediction of current work and the numerical data of Subramanian et al. (2017) confirms that the mesh system and numerical setup are convincing in the simulation of flow over a VAWT.

The variation of power coefficient with tip speed ratio, shown in Figure 14, confirmed that the CFD results are in line with the data presented by Subramanian et al., (2017), McLaren

(2011) and Bose et al. (2014). In current study, the tip speed ratio starts at medium low tip speed ratio, λ=1.3, and power coefficient at this point is close to all the pervious results. The difference between current simulation and Bose et al. (2014) (2D simulation) and Subramanian et al. (2017) (3D simulation) is around 7.7%. The peak value of power coefficient occurs at λ=2.3, which is the same as Bose et al. (2014); however, it is about 4.2% compared to Subramanian et al. (2017). The good agreement observed for different tip speed ratios reveals that the current settings can provide a reasonable prediction of the turbine performance. Figure 15 shows the velocity field for three relevant positions of the blade at different azimuthal angles such as $\theta = 0°$, 120°, and 240° during the revolution.
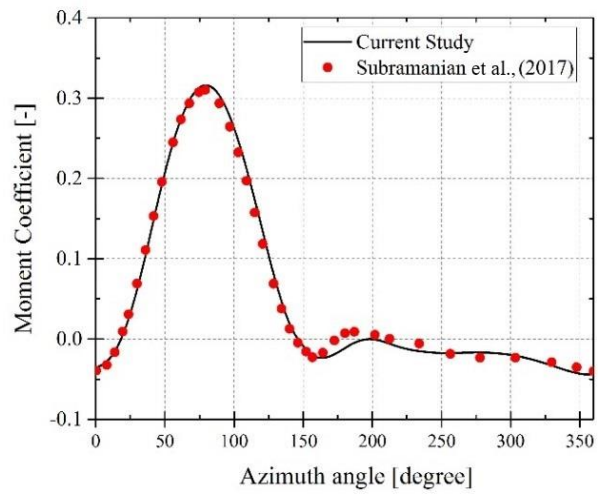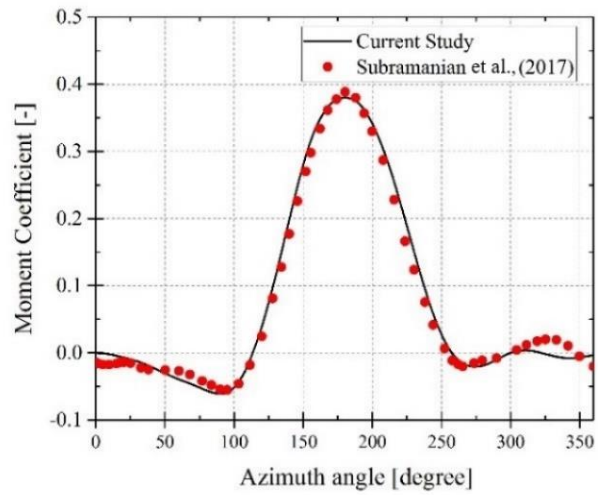
Figure 13. A comparison between the current study and the numerical data of the moment coefficient of blade1 in 2-blade (top) and 3-blade (bottom) turbine with tip speed ratio of 2.5 presented by Subramanian et al. (2017).
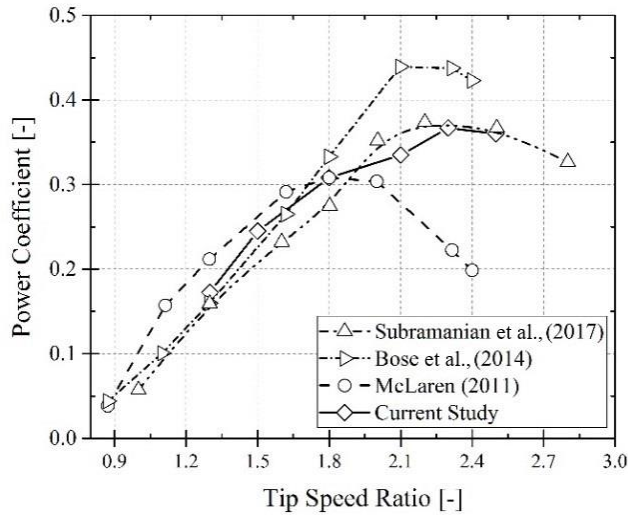
Figure 14. A comparison between the current study and the numerical data of the power coefficient with Tip Speed Ratio presented by Subramanian et al. (2017), McLaren (2011), and Bose et al. (2014).

(a)	(b)
(c)	(d)
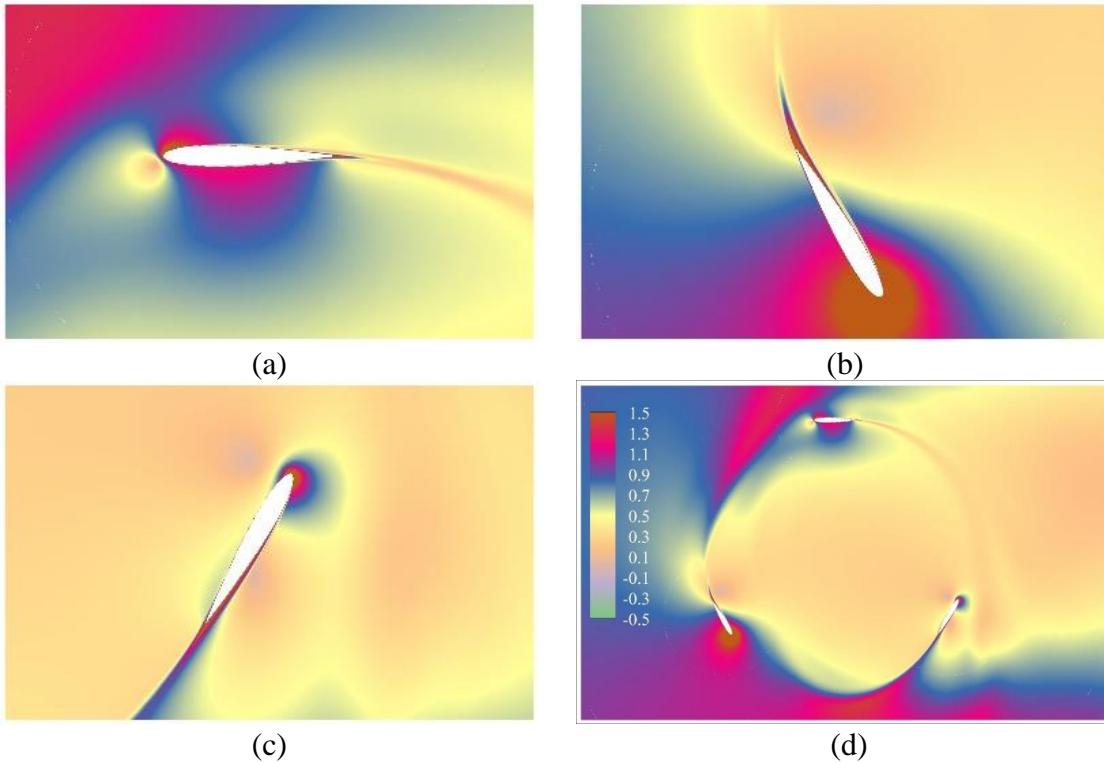
Figure 15. The velocity contour at different azimuthal angles (a) $\theta = 0°$ (b) $\theta = 120°$ (c) $\theta = 240°$, and (d) overall view.

31

3.3.2 Validation for flow-driven turbine

In the second validation study, the wind turbine is left to rotate freely based on the torque experienced over time with activated six DOFs. The purpose of this validation is to verify the vertical turbine capability to free spin and to check the angular velocity limit without adding any loads. Contrary to first validation, a moment of inertia is required for second validation case to make sure wind turbine can accelerate properly. A small value of 0.018 kg.m^2 is chosen as rotor moment of inertia under recommendations of Rainbird (2007) and Asr et al. (2016). A small value of moment of inertia will not affect the peak tip speed ratio value because the equilibrium point is not affected by acceleration term, but it can help the reduction of simulation time and get the acceleration trend of turbine quicker. The computational parameters of this case are given in Table 2.

Table 2. Main features of the validation for flow-driven turbine simulation.

Parameter	
Airfoil profile	NACA0018
Chord Length, c [m]	0.083
Rotor Diameter, D [m]	0.75
Freestream velocity, U_∞ [m/s]	6
Blade Length [m]	1
Rotor Axis Diameter [m]	0.04
Number of Blades [-]	3
Rotor Moment of Inertia [kg/m^2]	0.018

The inlet is 6 m/s in order to compare the results with data presented by Rainbird (2007), Rainbird (2016), Hill et al. (2009), Bianchini et al. (2011), and Chua (2002). The turbulent intensity of 1% and viscosity ratio of 10 are also selected for in this case. The six DOFs solver is adapted in the second validation and all other free-to-spin cases.

Figure 16 shows a comparison between the numerical predictions of the tip speed ratio time series of turbine start-up period, and the corresponding numerical data obtained by other

numerical and experimental results by Rainbird (2007), Rainbird (2016), Hill et al. (2009),

Bianchini et al. (2011), and Chua (2002). It is observed that the tip speed ratio time series has the

similar values and trend at both acceleration stage, but it reaches a 9% higher steady state value

compared to Bianchini et al. (2011). A quasi−steady of turbine at the beginning produces the first

stage acceleration, and then turbine comes into a discrete thrust−producing, which is a relative

stable plateau. In the last stage, called full lift−driven state, there is a continuous thrust producing

a second acceleration until the turbine reaches peak speed of 59.59 rad/s, which is smaller than

68 rad/s reported by Asr et al. (2016). Figure 16 shows that substantial improvement is achieved

compared to the other numerical and experimental.
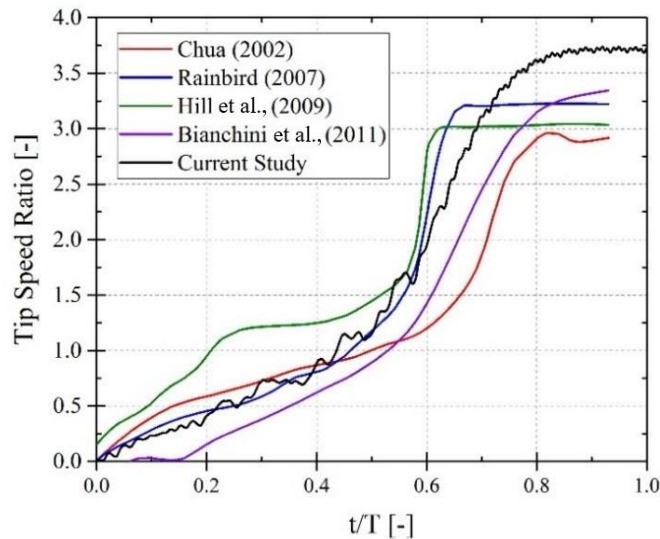
Figure 16. A comparison between the current study and the numerical data of Tip
Speed Ratio versus non-dimensional time presented by Rainbird (2016), Hill et al.
(2009), Bianchini et al. (2011), and Chua (2002).

3.4. Independence test for hydropower turbine

3.4.1 Grid independency

In grid independence test for hydropower turbine, three grid systems namely coarse

mesh, medium mesh and fine mesh are tested and results are deemed grid independent when the

difference in the torque coefficient, C_T, as a function of the rotor azimuth is negligible between

three consecutive tests. Torque coefficient is a good choice to test grid independence since it

shows the turbine performance at every single position. For the same domain size, results are

generated for a turbine, first with 412,782 nodes followed by 533,068 nodes (1.3 times denser

than coarse mesh), and 693,703 (1.3 times denser than medium mesh). Figure 17 shows the

variation of torque coefficient versus Azimuth angle at three different grid systems.
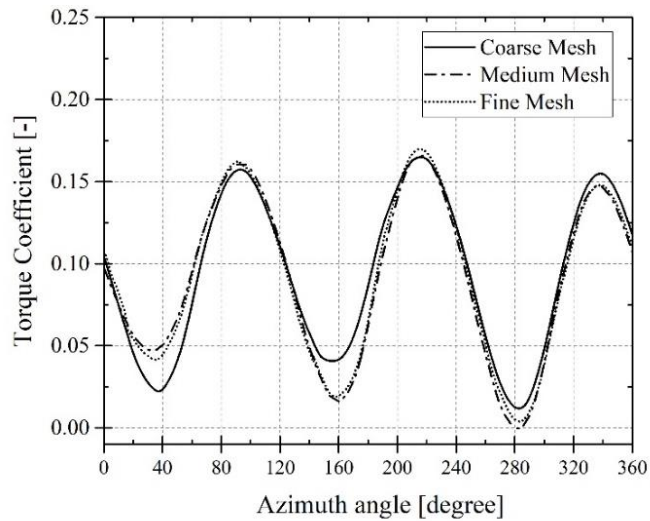
Figure 17. The variation of torque coefficient versus Azimuth angle at three different
grid systems of hydropower turbine.

After eliminating transient effects, the difference between the torque coefficients in three

grid systems are compared and a negligible difference is found between medium and fine mesh.

It can be seen that the minimum value of the C_T corresponding to coarse mesh is much lower

than that of medium and fine mesh, and the trend of C_T corresponding to medium and fine mesh

are almost identical. Due to this result, the medium mesh with 533,068 nodes is chosen for all

simulations as an appropriate choice for the calculation accuracy and cost.

3.4.2 Time step independency

Since all simulations are unsteady computation, finding a proper time step can significantly affect the cost and accuracy of simulation. A too large time step can lead into unrealistic results, and choosing a very small size of time step could increase the calculation cost. In most wind power studies, it is recommended to use a range from 1-degree to 2-degree motion during one-time step (Hwang et al., 2009; Bose et al., 2014; Subramanian et al. 2017). However, due to the presence of free surface in hydropower turbine, the 1-degree per time step is too large so that the free surface cannot be captured accurately. It is observed that even 0.5-degree per time step cannot capture the wave motion. Therefore, the 0.25-degree motion during one-time step is chosen as the proper time step for all simulations. Figure 18 presents the torque coefficient versus angular position for three different degree per time step, 0.5 and 0.25, in submerged depth, $h/R = 1.2$ and tip speed ratio, λ=1.5 case. The torque coefficient difference can reflect power coefficient difference. Power coefficient corresponding to 0.5-degree and 0.25-degree motion during one-time step are 0.1141 and 0.0830, respectively, which has 27.28% difference.
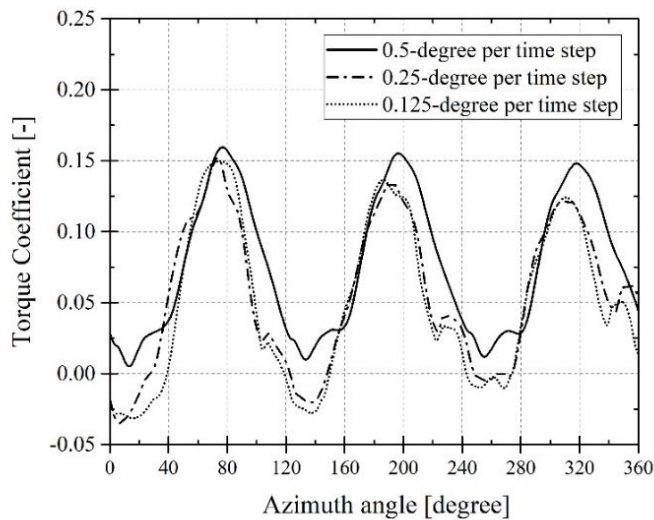
Figure 18. The variation of torque coefficient versus Azimuth angle at three different time steps of hydropower turbine.

CHAPTER 4 SIMULATION OF FLOW OVER SINGLE HYDROFOIL

Hydrofoil is widely used in many engineering applications such as hydropower energy harvesting, ships and submarines. In all these applications, an object is placed beneath the free surface and there is a fluid-structure interaction between free surface and the object with complex near-field fluid flow. Understanding this interaction is vital for designing energy harvesting devices or sail planes of submarines. In flow over a hydrofoil close to free surface, at a certain velocity level, a wave breaking occurs which causes the fluctuations of both lift and drag forces. This phenomenon can heavily affect the performance and behavior of the hydrofoil motion. Thus, it is important to simulate the interaction of hydrofoil-free surface to predict the force on hydrofoil. Although fluid-structure interaction in flows past objects near free surfaces has been a popular topic in recent decades and it was investigated by other researches (Miyata et al., 1990; Whelan et al., 2009; Birjandi et al., 2013; Wu et al., 2014; Filippas and Belibassakis, 2014; Riglin et al., 2015; Liu et al., 2016; Bouscasse et al., 2017), there are no comprehensively numerical researches to discuss flow field and the hydrodynamic loadings. Therefore, that is a major motivation of this work which could be a practical research for applications such as hydropower turbine close to free surface or marine vehicles.

While some attention has been focused on flow over hydrofoil near the free surface, the understanding of the free surface effect and its interaction with near-surface hydrofoil has not yet been studied in detail. Therefore, the primary objective of this work is to use computational fluid dynamics (CFD) method to investigate the hydrodynamic forces on the hydrofoil and the change of nearfield flow. Two sets of validation will be carried out to validate the modelling methodology. Submerged depth (h/c) and attack of angles (AOA) will be two main variables in

36

this work. The drag and lift coefficients as two important parameters in performance of hydrofoil and fluid flow as a function of submerged depth will be investigated.
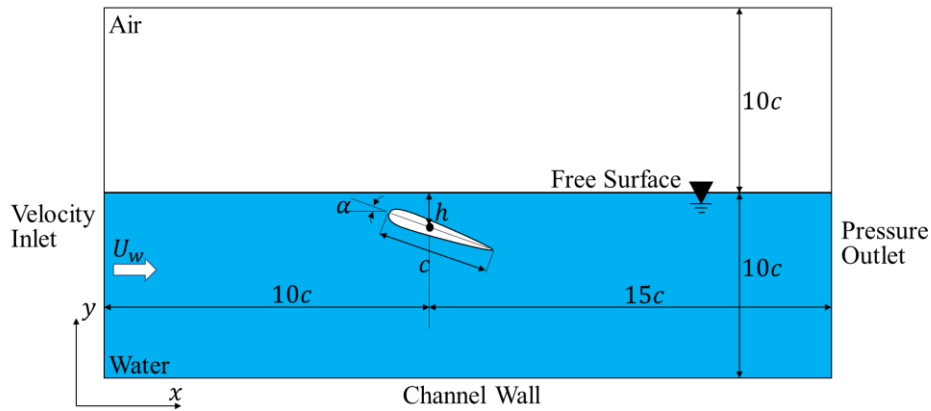
Figure 19. Schematic of the hydrofoil under free surface.
4.1. Mathematical modeling of flow over hydrofoil

4.1.1. Physical problem description

The simulations are performed in a two-dimensional domain. A basic schematic of the problem is shown in Figure 19, along with important dimensions. To facilitate the analysis, a Cartesian coordinate system is used with x pointing downstream, and y pointing upward. The origin of the coordinate system is located at the center of hydrofoil. As it is shown in this figure, a hydrofoil with cross section of NACA0015 airfoil with chord length c is submerged in the fluid at the distance h beneath an undisturbed free surface. The computational domain covers an area of $25c \times 20c$ in x and y directions, respectively, and it is split into two zones. Zone I represents air side with dimension of $25c \times 10c$, while zone II represents the water zone with the same dimension as zone I. The hydrofoil stands at $10c$ to the downstream of the inlet. In the downstream of the hydrofoil, $15c$ is reserved for the development of free surface and wake flows.

37

The depth to chord length ratio is defined as h/c. The fluid flow is from left to right which involves the two-fluid phases including stationary air as primary fluid and water as secondary fluid entering into the domain with the uniform stream velocity, U_w. The fluids have the constant properties including densities (ρ_a for air and ρ_w for water), and the dynamic viscosities (μ_a for air and μ_w for water). A list of all the geometrical and operational parameters used in the simulations is presented in Table 3.

Table 3. Geometrical and operational characteristics of the hydrofoil.

Parameter	
Hydrofoil profile	NACA0015
Chord length, c [m]	1
Submerged depth, h [m]	0.2, 0.3, 0.5, 0.7, 0.9
Froude numbers [-]	0.1, 0.3, 0.6, 0.9
Reynolds numbers [-]	$3.12{\times}10^5$, $9.37{\times}10^5$, $1.8{\times}10^6$, $2.8{\times}10^6$
Angle of attack, α [degree]	-15, -10, -5, 0, +5, +10, +15

4.1.2. Grid system of hydrofoil

In numerical simulation, a high-quality grid system can enhance the efficiency of calculation, the accuracy of solution, and the robustness of convergence. In the process of mesh generation, boundary layer grids close to solid surfaces become more important for complex flow structure. To accurately simulate the flow of the airfoil, refined grids are used in the boundary layer of airfoil. In order to create an appropriate grid system around the boundary layers, y^+ theory is employed. Based on theoretical derivations and experimental explorations, the boundary layers are classified into four parts including viscous sub-layer ($y^+ \leq 5$), buffer layer ($5 < y^+ \leq 30$), log-law region ($30 < y^+ \leq 500$), and outer layer (Versteeg and Malalasekera, 2007). The y^+ is defined as:

$$y^+ = \frac{u_\tau y}{\nu} \tag{4.1}$$

where u_τ is the friction velocity defined as:

$$u_\tau = \sqrt{\tau_w/\rho} \tag{4.2}$$

where ν is the kinematic viscosity, y represents the height of the grid to wall, τ_w denotes the wall

shear stress, and ρ is the fluid density.

The grid system has a strong impact on the model accuracy, and a high-quality grid

system enhances the efficiency of calculation, the robustness of convergence, and the accuracy

of solution. In this study, a structured grid system is generated for the computational domain, as

shown in Figure 20. The hydrofoil is considered to be rigid, and its surface is considered to be a

wall. In the process of mesh generation, boundary layer grids close to solid surfaces are always

the focus of much attention. To accurately simulate the flow of the airfoil, refined grids are used

in the boundary layer of airfoil. Of particular importance is modeling the boundary layer in

sufficient detail by covering relevant boundaries with at least 10 layers of cells; this allows the

chosen turbulence model to achieve its calibrated performance (ANSYS user guide, 2018). The

computational mesh system is shown in Figure 20. The grid system for $\alpha = +5°$ has 537,070

cells. The primary concentration of this mesh system is alongside the free surface and the area

around the hydrofoil. The desired y^+ for this case is about 1 that is enough for catch the

boundary layer properties, which means the closest two grid points should be distanced by

0.00005m in this case. The mesh is set by biased near the free surface and cylinder. The mesh

system for the area far away from the free surface can be looser, because the physical parameters

will not change a lot in the rest areas.
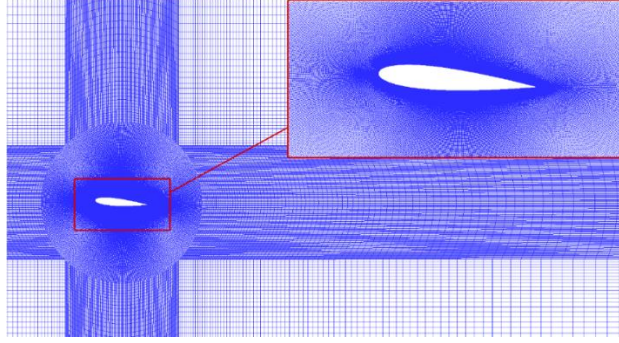
Figure 20. The grid system in entire domain and a close-up view of the grid near the hydrofoil for $\alpha = +5°$.

4.1.3 Boundary and initial conditions

Two different inlets are defined for air flow and water flow in the computational domain. These two inlets are defined as stream-wise velocity inlets that need the values of velocity. The lower boundary below the water phase and hydrofoil wall are specified as a no-slip condition, and the law of the wall function is applied to the SST $k - \omega$ turbulence model. Moreover, the upper boundary in computational domain and above the air phase is specified as a symmetry condition, which enforces a zero normal velocity and a zero-shear stress, causing it to behave as open to atmosphere. Finally, a gauge pressure of zero is applied at the outlet using the outlet pressure boundary condition. Since this is a two-phase flow of air and water, at the inlet and the outlet of water phase, the free surface level is defined in the VOF model based on the hydrofoil depth. Since the VOF method is used to capture free surface, there is no need to set the kinematic and dynamic free surface boundary conditions.

At the initial time of simulations, the air flow is set to zero while the water flow is set the same as inlet flow. The value of volume fraction is set as 0 for the all cells in air phase and value of 1 for the cells in water phase. The hydrostatic pressure is also initialized in the computational domain.

4.1.4. Simulation setup

The simulation is conducted by using computational fluid dynamic software ANSYS Fluent Version 19.2. For coupling between velocity and pressure, SIMPLE algorithm is employed, and skewness correction is set as 1. As mentioned before, SST $k - \omega$ turbulent model is applied to capture the turbulence flow. The transient formulation is first order implicit. The pressure scheme is PRESTO as recommended, and the momentum, turbulent kinetic energy, and specific dissipation rate are all solved by second order upwind. The results of the numerical simulation converge when the scaled residual is less than 10^{-4}. The free surface is defined by a value of $\alpha = 0.5$. (ANSYS user guide, 2018). For the unsteady-state calculation, the time step was found to be sufficiently small to give relatively good convergence for the equation residuals, and both the computing hardware and computing time must be considered. Therefore, the time step is set as 0.0025s to make sure the courant time is relatively small for convergence.

In the application of hydropower turbine, it is important to find out how much energy can be extracted from flow current. This can be done by determining the force including life and drag forces acting on the blades. The lift and drag forces can be obtained as:

$$F_L = \frac{1}{2}\rho C_L U_w^2 A \qquad (4.3)$$

$$F_D = \frac{1}{2}\rho C_D U_w^2 A \qquad (4.4)$$

where C_L is the lift coefficient, C_D is the drag coefficient, and A is the area of the immersed object projected over the incoming flow.

4.2. Flow past a hydrofoil in vicinity of free surface

Simulations are performed for a multiphase flow past a hydrofoil beneath a free surface with various submerged depths, Froude numbers and angles of attack using the VOF with the

SST $k - \omega$ turbulence model. The chord length of hydrofoil is assumed to be constant for all cases. The simulations are performed in a two-dimensional domain. Note that some three-dimensional simulations are also done in few cases and it is found that two- and three-dimensional domains lead to a negligible difference (less than 2%) in the calculated hydrodynamics performance for the studied operating conditions. An example of three-dimensional simulation for the case of $h/c = 0.3$, $Fr = 0.3$, and $\alpha = +5°$ is shown in Figure 21.
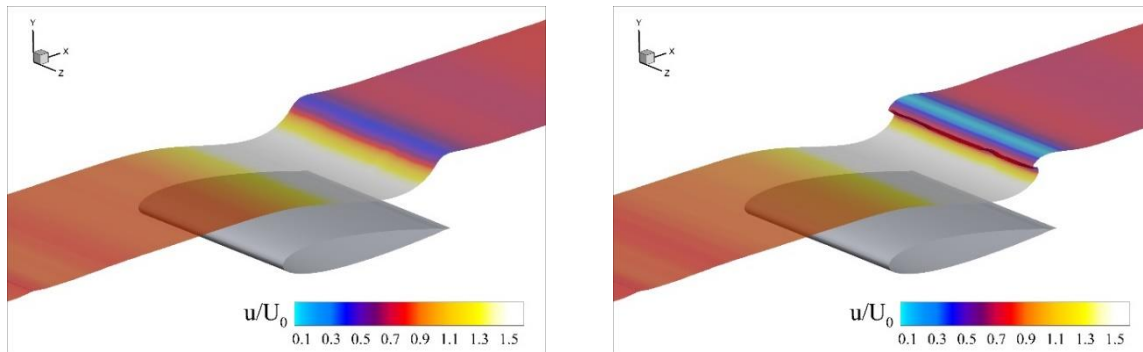
Figure 21. Instantaneous contour of the water volume fraction colored with velocity magnitude for the $h/c = 0.3$, $Fr = 0.3$ and 3 angle of attack $\alpha = +5°$.

The angle of submerged hydrofoil near free surfaces could be an integral part of the design and optimization of hydropower systems. Flow visualization reveals that the interaction of hydrofoil with the free surface is profoundly influenced by the angle of hydrofoil. Hence, hydrodynamic loadings are expected to be a strong function of the angle of hydrofoil. The effect of hydrofoil angle on free surface can be seen in Figure 22. Instantaneous contours of the water volume fraction at $h/c = 0.2$ and $Fr = 0.3$ for different angles of attack are depicted in this figure. It is observed that the free surface characteristics for positive angles of attack significantly differ from those for negative angles. For $\alpha \geq 0$, the free surface level rises near upstream of the hydrofoil and dips rapidly at the middle of the hydrofoil which results in jet formation immediately at the middle of hydrofoil.
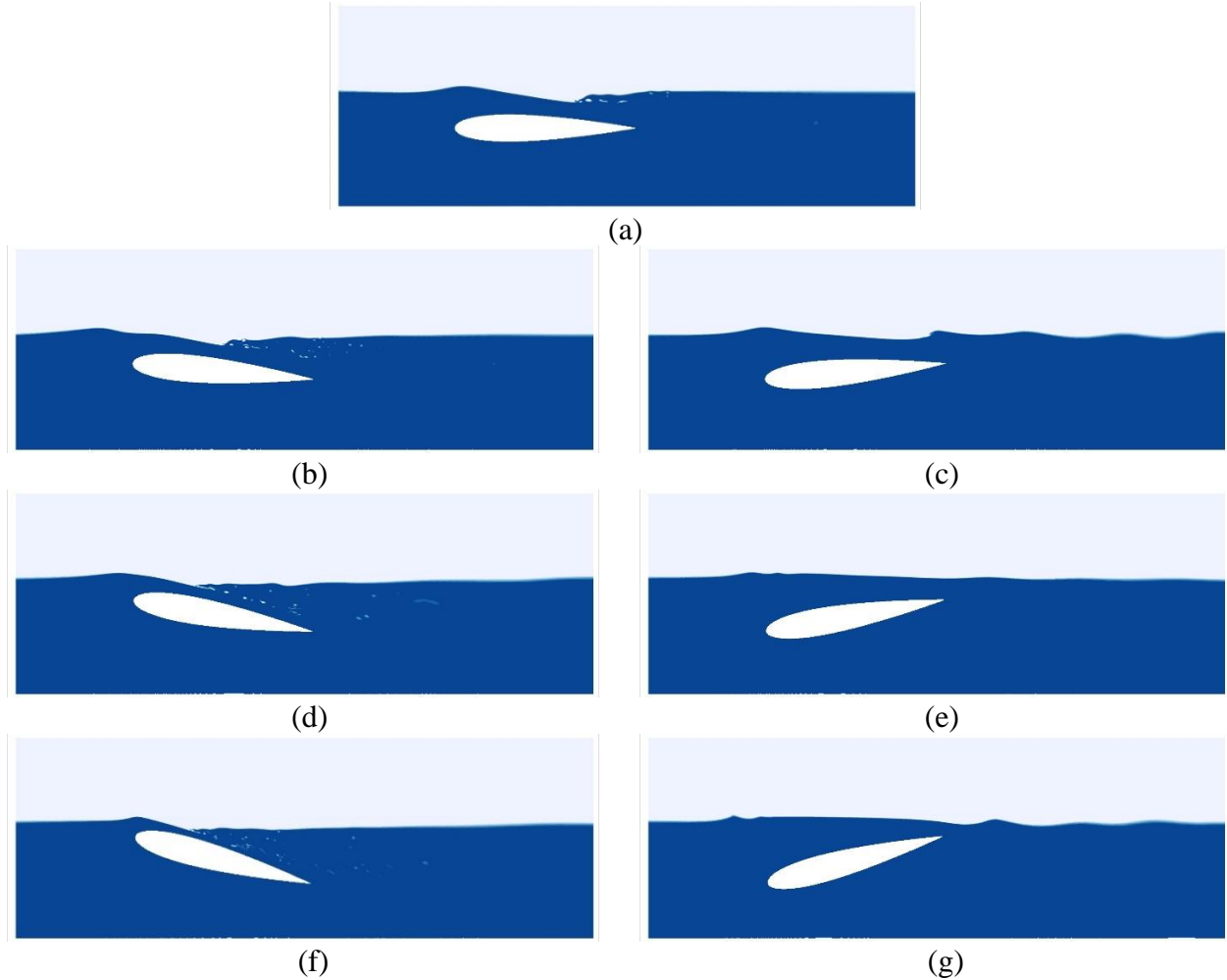
Figure 22. Instantaneous contour of the water volume fraction for the $h/c = 0.2$, $Fr = 0.3$ and various angles of attack (a) $\alpha = 0°$, (b) $\alpha = +5°$, (c) $\alpha = -5°$, (d) $\alpha = +10°$, (e) $\alpha = -10°$, (f) $\alpha = +15°$, (g) $\alpha = -15°$.

Due to the free surface deformations induced by the free surface and hydrofoil interaction, the air entrainment phenomenon occurs which can be clearly observed for zero and positive angles of attack in the region between the hydrofoil and free surface. Once the air entrainment occurs, the penetrated air convects downstream of the hydrofoil, as it can be seen in Figure 22. Air penetration over the hydrofoil is more intense for higher angles of attack, while the amount of entrained air decreases as the angle of attack is decreased. For $\alpha < 0°$, the free surface in all cases tends to stay undisturbed and the amount of penetrated air is much less compared to that for $\alpha \geq 0$.
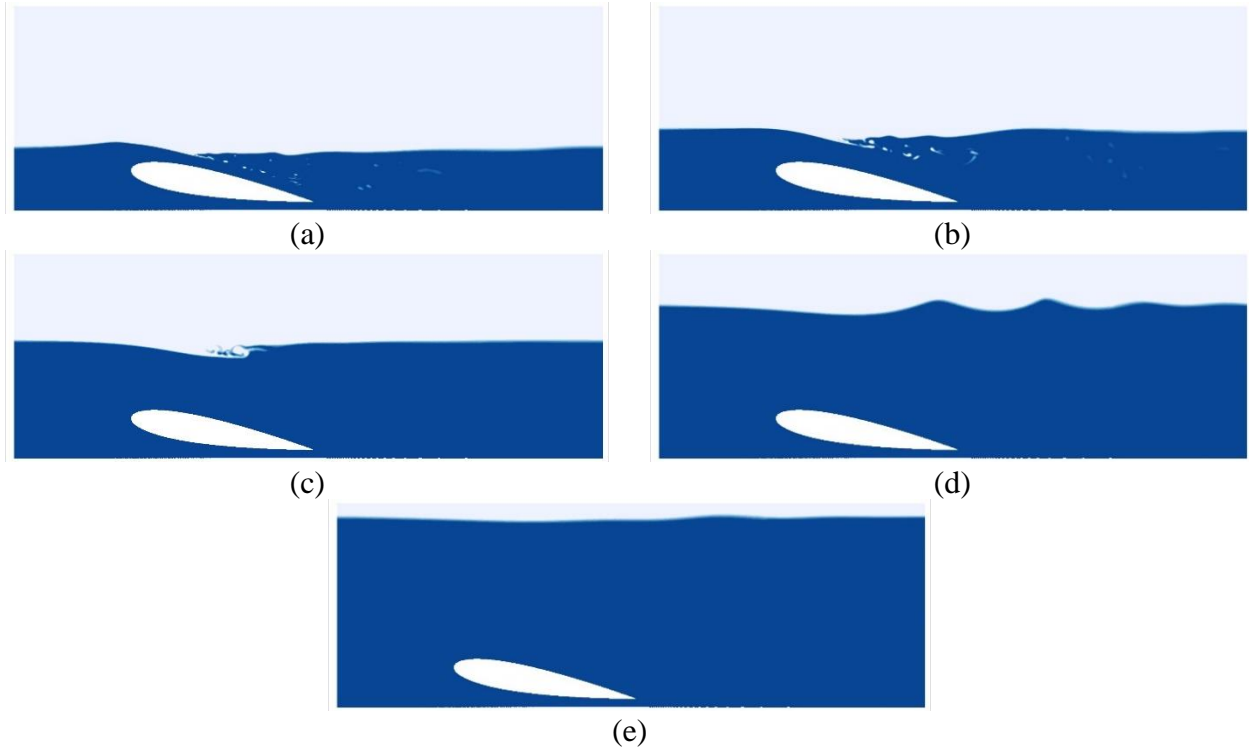
Figure 23. Instantaneous contours of the water volume fraction for the $Fr = 0.3$, $\alpha = +10°$, and various submerged depths (a) $h/c = 0.2$, (b) $h/c = 0.3$, (c) $h/c = 0.5$, (d) $h/c = 0.7$, and (e) $h/c = 0.9$.

Figure 23 shows the effect of submerged depth on the flow structure. For constant $Fr = 0.3$ and $\alpha = +10°$, the submerged depth varies from $h/c = 0.2$ to 0.9. It is interesting that for $h/c = 0.2$ and 0.3, the jet generated on top of hydrofoil caused a wave breaking at the middle of hydrofoil. As the submerged depth increases, the jet disappears, however, the amplitude of the downstream wave starts to increase. The largest free surface elevation occurs in submerged depth of $h/c = 0.7$. Regarding the wave trough, its depth decrease as the submerged depths is increased to $h/c = 0.9$.

The computations have been performed for four different Froude numbers $Fr = 0.1$, 0.3, 0.6 and 0.9 in order to examine the influence of the Froude number on fluid flow. The results of these computations are presented in Figure 24. According to Eq. (3.2), Froude number is calculated in respect to the hydrofoil chord length and advance speed. For the lower advance

speed case that correspond to low Froude number of $Fr = 0.1$, the free surface presents very

small wave amplitude and no wave breaking occurs on the free surface. For the higher advance

speed cases corresponding to $Fr = 0.3$ and 0.6, it is noticed that a jet is generated on the free

surface, above the hydrofoil, which remains parallel to the surface of hydrofoil and causes an air

entrainment at the middle of the hydrofoil; implying that the free surface deformation and the

structure-fluid interaction can be affected by Froude number. For Froude number of $Fr = 0.9$,

no air entrainment occurs close to the hydrofoil. However, the free surface presents large wave

amplitude; a wave breaking happens further downstream of the hydrofoil.

(a) (b) (c) (d)
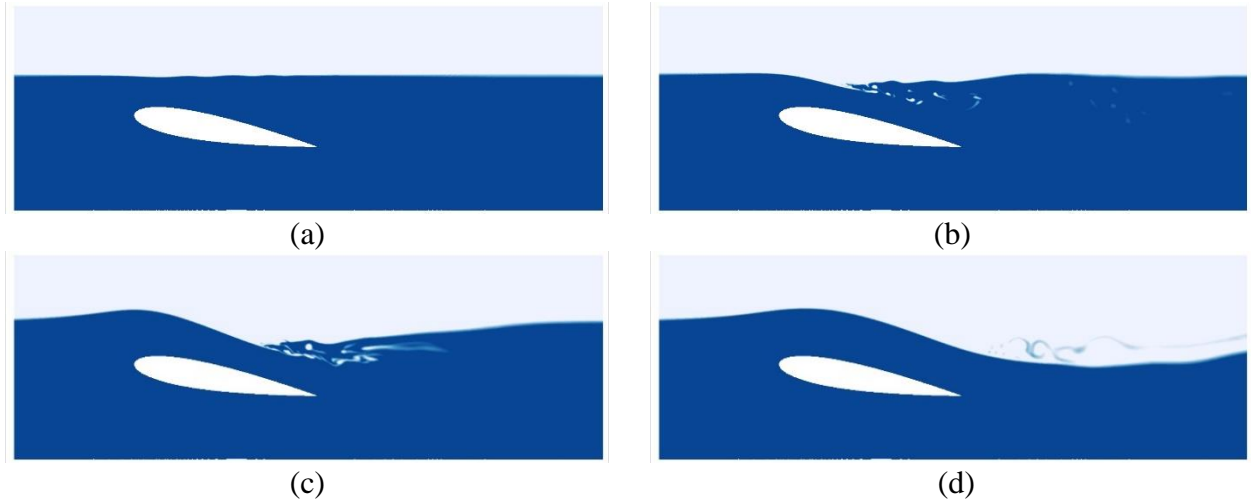
Figure 24. Instantaneous contours of the water volume fraction for the $h/c = 0.3$, $\alpha = +10°$, and various Froude numbers (a) $Fr = 0.1$, (b) $Fr = 0.3$, (c) $Fr = 0.6$, and (d) $Fr = 0.9$.

A sequence of frames showing the evolution of complex interface evolutions including

wave breaking or air entrainment is shown in Figure 25. The counters are colored by normalized

velocity magnitude. It is observed that a coanda-like flow is established on top of the hydrofoil

which results in a layer of fluid getting attached to the top part of the hydrofoil as a jet flow and

projects it into the bulk of the fluid. Due to this, an overturning wave with strong vertical

velocity component is formed downstream of the hydrofoil.
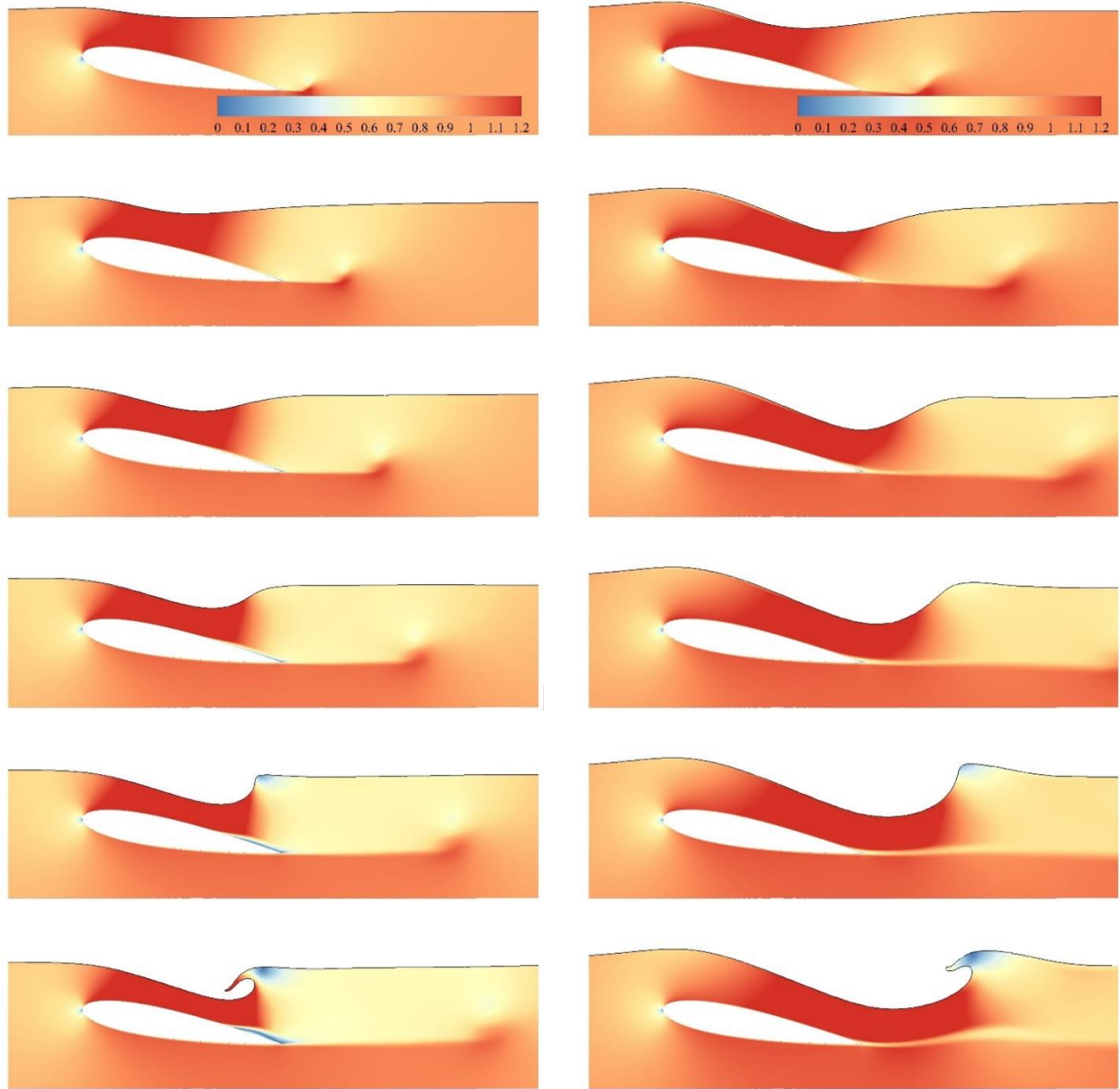
Figure 25. The evolution of free surface including wave formation for (left) $h/c = 0.3$, $Fr = 0.3$, and $\alpha = +10°$; (right) $h/c = 0.3$, $Fr = 0.6$, and $\alpha = +10°$. Contours are colored by normalized velocity magnitude.

It is observed that the position of this overturning wave strongly depends on submerged depth and Froude number. On further propagation, the overturning wave develops into a plunging jet with formation of air pocket and impinges on the first jet flow which results in air entrainment phenomenon. Also, a second jet due to the splash-up of impinging jet and its

plunging can be formed. The interaction of these two jets in flow over hydrofoil is beyond the scope of this work. The structure of jet flow on top of the hydrofoil for different angles of attack is shown in Figure 26.
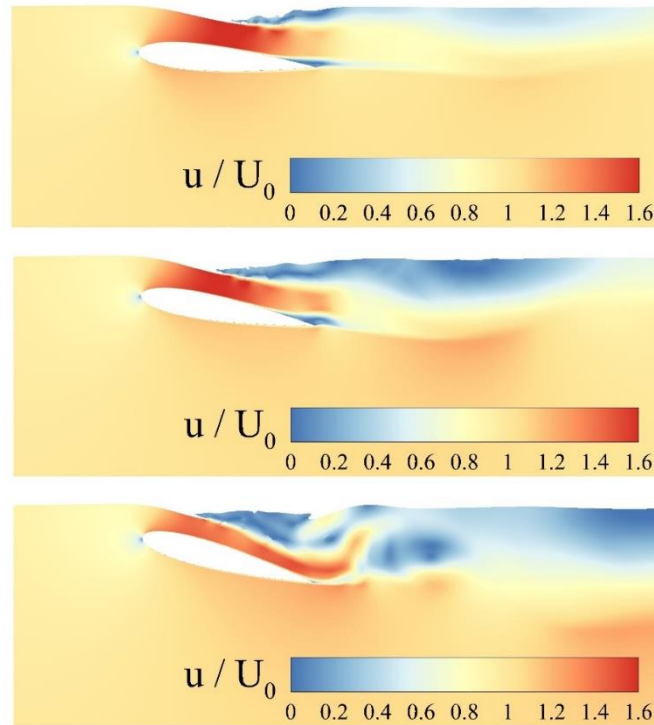
Figure 26. The structure of jet flow on top of the hydrofoil for at $h/c = 0.3$, $Fr = 0.3$ and different angles of attack (top) $\alpha = +5°$, (middle) $\alpha = +10°$, and (bottom) $\alpha = +15°$.

4.3. Hydrodynamic force characteristics

The values of average lift and drag coefficients with different angles of hydrofoil and various submerged depths at $Fr = 0.3$ are compared and shown in Figure 27. Figure 27a shows that the average lift coefficient increases with the same slope in all submerged depths up to $\alpha = 0°$. By increasing the angle of attack from $\alpha = 0°$ to $+15°$, this increasing continues with the same slope for $h/c = 0.5$, 0.7 and 0.9, while in the cases of $h/c = 0.2$ and 0.3 the lift coefficient tends to increase very slowly. Furthermore, according to Figure 27b, for negative angles of attack up to $\alpha = 0°$, it can be observed that the average drag coefficient slightly

changes in all submerged depths, and very little difference in average drag coefficient can be observed in all different submerged depths. However, for positive angles of attack, the average drag coefficient starts increasing in all submerged depths.

The time histories of lift and drag coefficients at $h/c = 0.3$, and $Fr = 0.3$ are shown in Figure 28 for various angles of attacks. The coefficients are calculated starting at 20s by using the instantaneous data at every 0.025 seconds. The trend of both coefficients implies that the force coefficients have reached stability. The results reveal that as the angle of attack increases, a periodic behavior is observed in both coefficients due to the wave breaking on the free surface, and the structure of vortex for $\alpha = 0°$ is distinctly different from those for $\alpha = +15°$. The variation of hydrodynamics forces with Froude number is shown in Figure 29. The results show that in a fixed angle of attack, the average life coefficient for both $h/c = 0.3$ and 0.7 decreases with the increase of Froude number. The same behavior is observed for drag coefficient when the hydrofoil is placed at $h/c = 0.3$ and this coefficient decreases as Froude number increases. However, at deeper submerged position of $h/c = 0.7$, the average drag coefficient corresponding to the $Fr = 0.6$ has higher value respect to the ones for $Fr = 0.3$ and 0.9.

<div align="center">(a)   (b)</div>
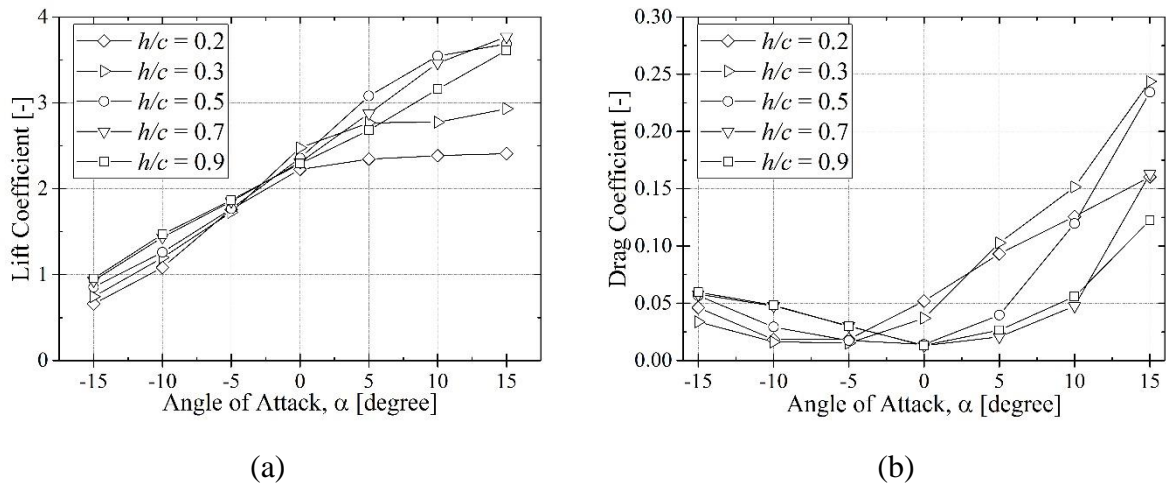
Figure 27. The average (left) Lift and (right) Drag coefficient versus angle of attack for various submerged depths and $Fr = 0.3$.
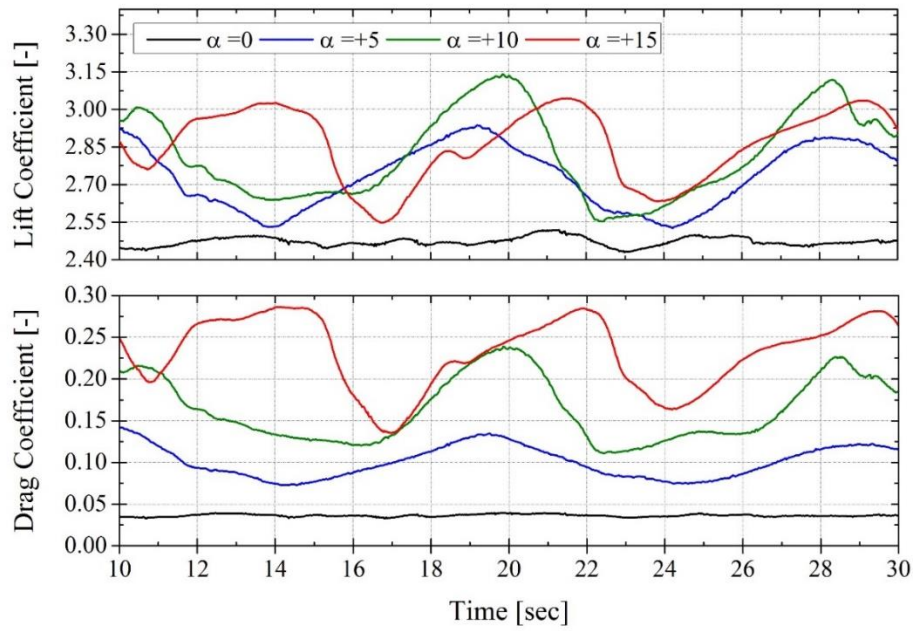
Figure 28. The instantaneous (top) lift and (bottom) drag coefficients for various angles of attack at $h/c = 0.3$ and $Fr = 0.3$.
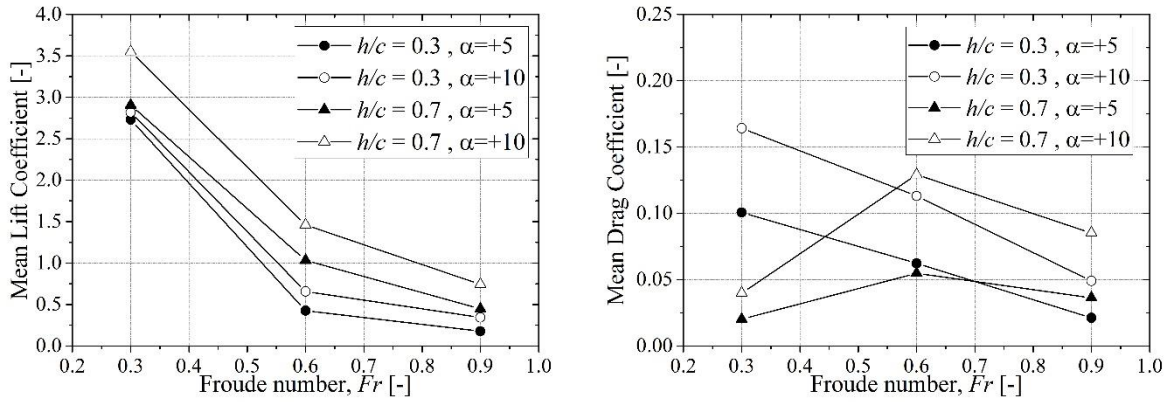
Figure 29. The average (top) lift and (bottom) drag coefficient versus Froude number for different submerged depths and angles of attack.

4.4. Wave profile over free surface

To examine the effect of angle of attack on the flow condition around the hydrofoil, the free surfaces of different angles of attack are presented in Figure 30. The wave profile of all angles of attack are calculated at the time right before the wave breaking occurs. The position of the free surface is determined by the location of the volume fraction of 0.5 in computational domain. The hydrofoil is located at the submerge depth of $h/c = 0.2$ and the Froude number for all angles is $Fr = 0.3$, which the flow condition covers subcritical flow. The angle of attack is in the range of $\alpha = -15°$ to $+15°$, and wave breaking occurs for both negative and positive angles of the hydrofoil. It is observed that the free surface is less disturbed in negative angles of attack; however, by increasing the angle of attack to $\alpha = +15°$ the free surface level in front of the hydrofoil and the amplitude of the wave disturbance behind the hydrofoil increases. Therefore, the wave elevates by the hydrofoil and dropped behind it. By placing the hydrofoil at $h/c = 0.3$, no wave breaking occurs in any negative angles. Therefore, the wave profile before breaking is meaningless for nonbreaking waves of negative angles. Figure 31 shows the wave profile for different angles at $h/c = 0.3$. Due to the presence of nonbreaking waves at negative angles, the wave profile of negative angles is not shown in this figure. As it is expected, the free surface

50

level in front of the hydrofoil and the amplitude of the wave disturbance behind the hydrofoil is

smaller than the ones of $h/c = 0.2$.
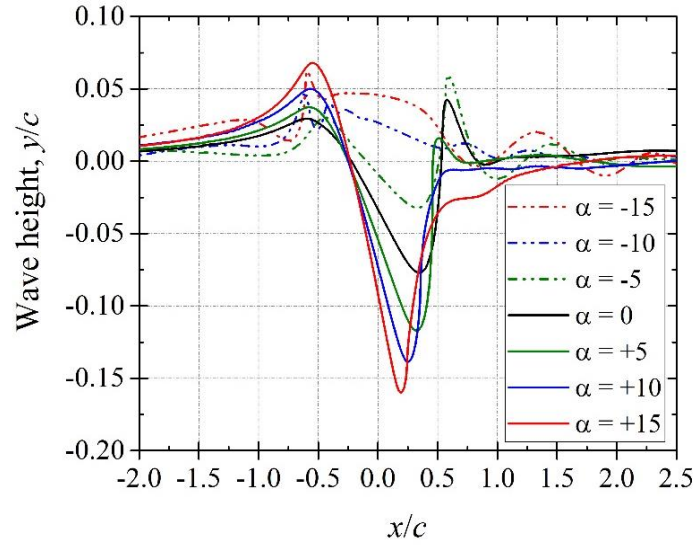
Figure 30. The wave profile before breaking for different angles of attack at $h/c = 0.2$ and $Fr = 0.3$.
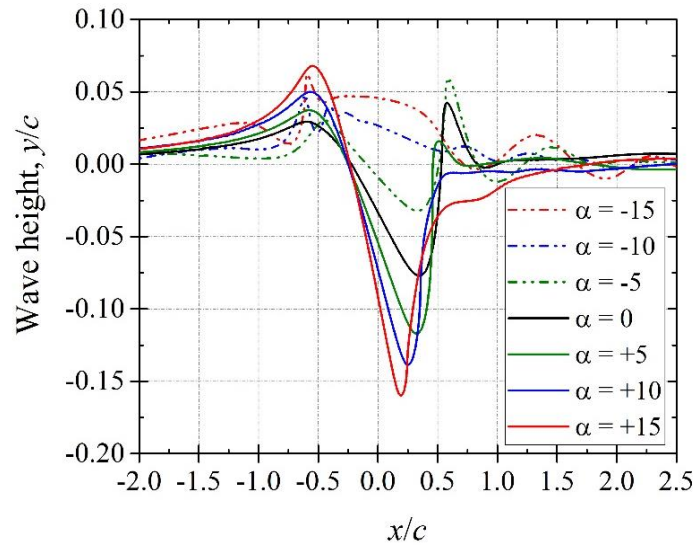
Figure 31. The wave profile before breaking for different angles of attack at $h/c = 0.3$ and $Fr = 0.3$.

Reviewing the results shows that wave breaking height is not always located at the top of

incident wave. Therefore, new parameters are needed to describe wave break in a quantitative

way. The height from free surface to wave break point is defined as breaker height (H_b), and

incident wave height (H_0) is defined as the distance from free surface level to the top of incident wave. The breaker height index (Ω_b) is defined as (Blenkinsopp and Chaplin, 2008):

$$\Omega_b = H_b/H_0 \qquad (4.5)$$

Some important wave heights and breaking wave kinematics parameters for submerged depths $h/c = 0.2$ and 0.3 are presented in Table 4 and Table 5, respectively. It should be noted that the values of H_0, H_b and x_b are nondimensionalized by chord length of hydrofoil in these Tables. For the negative angles of attack, wave breaking happens at the upstream only submergence depth is small. All the other breaking cases happen at the downstream. Therefore, wave breaking at downstream is much more common to occur, and the investigation of wave breaking in this section will focus on wave breaking at downstream. As Table 4 shows, the incident wave height, breaker height, and breaker height index decrease as the angle of attack increases. Also, the breaking position moves forward to upstream when the angle of attack increases. The trend of breaker height index varies with angle of attack which is shown in Figure 32. As can be seen in this figure, the breaker height index drops dramatically when angle of attack becomes larger than $\alpha = +5°$.

Table 4. Overview of different incident wave heights simulated, and related breaking wave kinematics for submergence depth $h/c = 0.2$ and $Fr = 0.3$.

Angle of attack, α [degree]	Incident wave height, H_0 [−]	Maximum breaker degrees	Breaking position, x_b [−]	Breaker height, H_b [−]	Breaker height index, Ω_b[−]
-5	0.2599	74.4137	0.5676	0.2525	0.9716
0	0.2440	70.1678	0.5199	0.2316	0.9493
5	0.2153	89.8810	0.4490	0.1964	0.9123
10	0.1952	77.1602	0.3531	0.1115	0.5712
15	0.1729	69.7252	0.2719	0.0519	0.3006

Table 5. Overview of different incident wave heights simulated, and related breaking wave kinematics for submergence depth $h/c = 0.3$ and $Fr = 0.3$.

Angle of attack, α [degree]	Incident wave height, H_0 [−]	Maximum breaker degrees	Breaking position, x_b [−]	Breaker height, H_b [−]	Breaker height index, Ω_b [−]
0	0.3567	71.2286	0.4048	0.3442	0.9650
5	0.3275	70.2891	0.3576	0.3116	0.9514
10	0.3011	66.1435	0.3500	0.2883	0.9573
15	0.2631	63.6147	0.2801	0.2085	0.7922
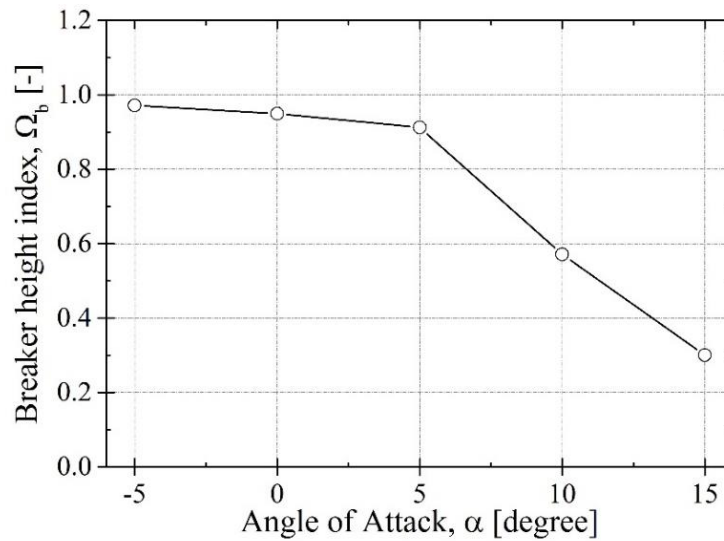
Figure 32. The variation of break height index for $h/c = 0.2$ with angle of attack.

Besides the effect of angle of attack on wave profile, submergence depth is another variable that can affect the wave profile in flow over hydrofoil beneath the free surface. Therefore, the angle of attack and Froude number are kept fixed at $\alpha = +5°$ and $Fr = 0.3$ to investigate the effect of different submergence depths in the range of $h/c = 0.2 − 0.9$. The result of this examination is presented in Figure 33. The results show that the wave is not breaking at submergence depth of $h/c = 0.9$ which also corresponds to Duncan (1981 and 1983) results. Therefore, the wave profile for this submerged depth is not presented in Figure 33. As this figure shows, the lowest wave height surrounding hydrofoil increases as submergence depth

increases. Also, the downstream wave shape is more disturbed when the submergence depth

reaches a certain point.
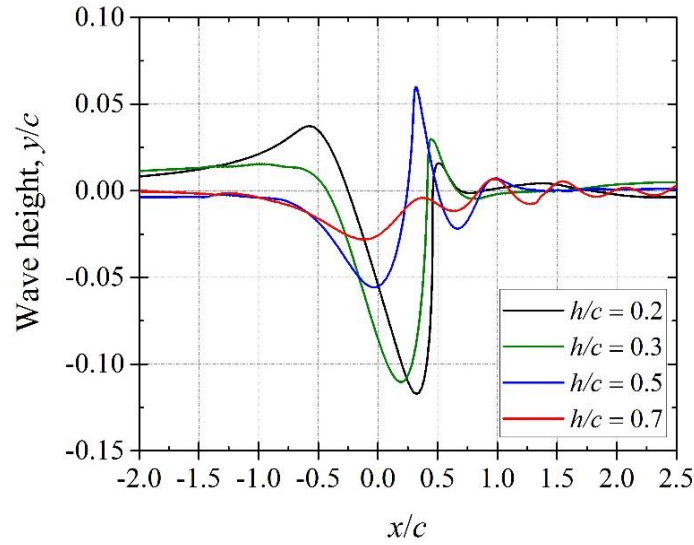
Figure 33. The variation of break height index for $h/c = 0.2$ with angle of attack.

Froude Number is another variable that can affect wave profile of flow. Figure 34 shows

wave profile before breaking for different Froude numbers at $\alpha = +5°$ and submerge depth of

$h/c = 0.3$. The wave break occurs only when Froude number is $Fr = 0.3$ and 0.6. It is noted

that no wave breaking occurs at $Fr = 0.1$ due to low input velocity of flow, and at $Fr = 0.9$ due

to deep position of hydrofoil. However, a significant distortion on the wave profile is observed at

$Fr = 0.3$, while this distortion is very small at $Fr = 0.1$. Comparing Froude number of $Fr = 0.3$

and 0.6, the wave has a larger amplitude, and wave breaking occurs farther downstream of

hydrofoil.
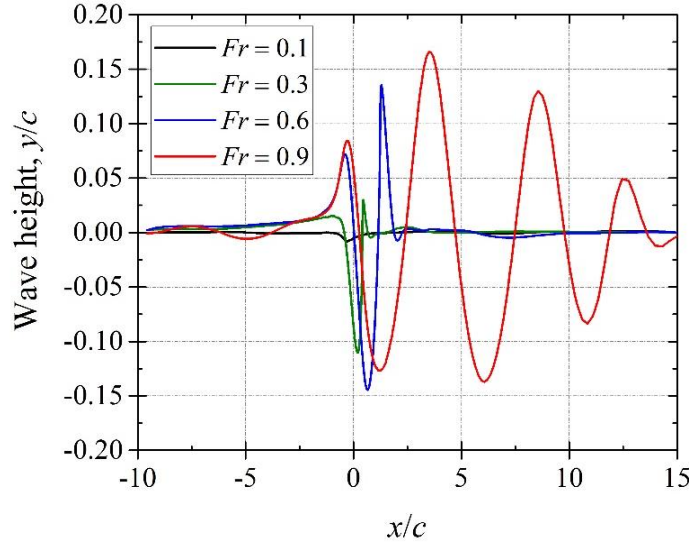
Figure 34. The wave profile before breaking for Froude numbers at $\alpha = +5°$ and $h/c = 0.3$.

The effect of Froude number on kinematics parameters of breaking wave is shown in Table 6. Only the results of two different Froude numbers are shown in this table, because the no wave breaking occurs at $Fr = 0.1$ and 0.9 as mentioned before. Table 6 shows the wave breaking type is basically the same which means the wave breaks have very similar break shape. According to this Table, both Froude numbers have similar breaking height index, while the breaking position occurs further downstream at $Fr = 0.6$.

Table 6. Overview of different incident wave heights simulated, and related breaking wave kinematics for submergence depth $h/c = 0.3$ and $\alpha = +5°$.

Froude number, Fr [-]	Incident wave height, H_0 $[-]$	Maximum breaker degrees	Breaking position, x_b $[-]$	Breaker height, H_b $[-]$	Breaker height index, $\Omega_b[-]$
0.3	0.3275	70.2890	0.3576	0.3116	0.9514
0.6	0.4390	70.9008	1.2385	0.4163	0.9484

4.5. Plunging jets

To describe the wave breaker type, Longuet-Hihhins (1982) provides a parametric method to quantitatively measure the cavity shape plunging jets. One sample of wave break and related parameters is shown in Figure 35. The length of cavity shape plunging jet is defined as l_v, and the

55

width of cavity shape plunging jet is defined as w_v. For length to width ratio as l_v/w_v, Blenkinsopp and Chaplin (2008) state a method to calculate the area enclosed by the curve which is presented as:

$$A_v = \frac{2\sqrt{3}}{5} l_v w_v \qquad (4.6)$$
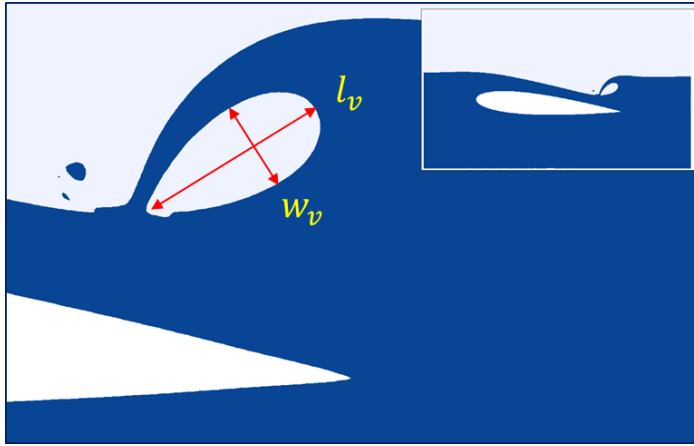
Figure 35. Wave breaking at the plunge point and cavity shape parameters.

As it is mentioned before, no wave breaking and as a result no plunging jets phenomenon occurs at negative angles of attack. Therefore, this section will focus on angle of attack in the range of $\alpha = 0° - 15°$. Figure 36 shows the measured cavity length to width ratio as a function of angle of attack for different submerge depths. Furthermore, Figure 37 presents the cavity area as a function of angle of attack for different submerge depths. For submergence depth greater than 0.5, the wave break does not have plunging jets. For instance, the wave break has obvious plunging jets at submergence depth $h/c = 0.7$ only when angle of attack is $\alpha = +15°$, even though the wave break occurs in other angles of attack. Therefore, Figure 36 and Figure 37 only show measured cavity length to width ratio and cavity area with submergence depth in range of

$h/c = 0.2 - 0.5$. The plunging jets have similar shapes in $\alpha = +15°$ for all three different submergence depth cases, however, they have different shapes in $\alpha = 0 - 10°$ for different submerged depths.
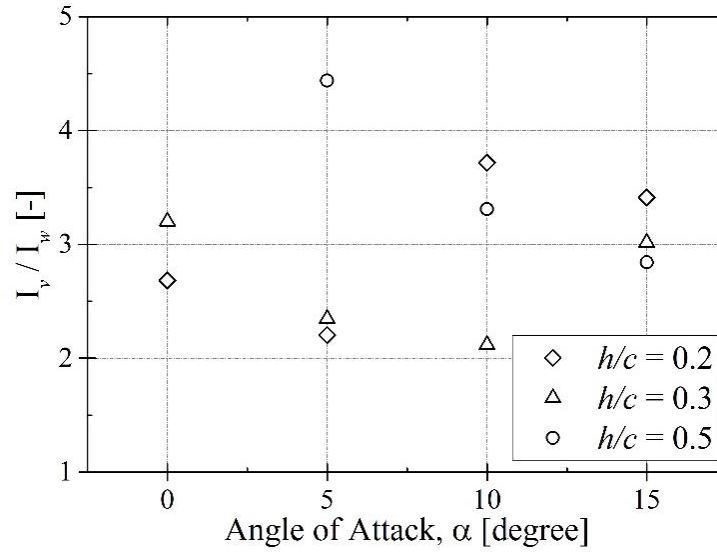
Figure 36. Measured cavity length to width ratio as a function of angle of attack for $Fr = 0.3$ and various submerged depths.
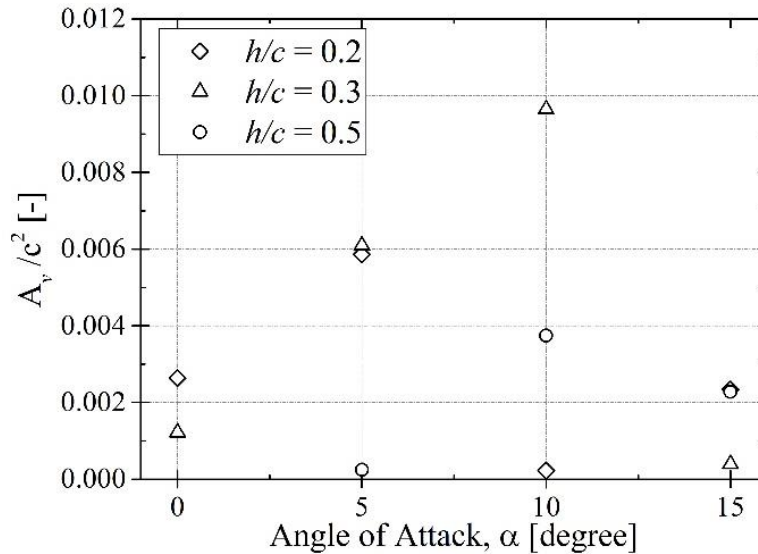
Figure 37. Cavity areas as a function of angle of attack for $Fr = 0.3$ and various submerged depths.

4.6. Wave breaking condition

Breaking condition is one of the key factors that affects the hydrofoil performance. Wave breaking causes the generation of high levels of turbulence, splash, and noise, which results in energy dissipation. For different angles of attack and for various submerge depths at Froude number of $Fr = 0.3$, Table 7 shows whether the wave breaks or not, and whether the wave breaking occurs in upstream or downstream of the hydrofoil. Compared to previous experimental results (Duncan, 1981 and 1983), it is obvious that the breaking condition is not only related to submerged depth, h/c, but also depends on the absolute submergence height, *h/c*.

Table 7. Breaking condition (U stands for wave breaking happens at upstream, D stands for wave breaking happens at downstream, and N represents no wave breaking happen but wavy wave).

Angle of Attack, α	$h/c = 0.2$	$h/c = 0.3$	$h/c = 0.5$	$h/c = 0.7$	$h/c = 0.9$
$-15°$	U	U	N	N	N
$-10°$	N	N	N	N	N
$-5°$	U	U	N	N	N
$0°$	D	D	D	N	N
$+5°$	D	D	D	D	N
$+10°$	D	D	D	D	N
$+15°$	D	D	D	D	N

4.7. Summary

Numerical simulations were performed to investigate the fluid-structure interactions between the free surface and hydrofoil. Varying submerged depths from center of hydrofoil to free surface for $h/c = 0.2, 0.3, 0.5, 0.7$ and 0.9, bulk flow velocities with corresponding Froude numbers (Fr) of 0.1, 0.3, 0.6 and 0.9 , and angles of attack of $\alpha = -15°$ to $+15°$ were studied. The multiphase VOF model and SST $k - \omega$ turbulence model were implemented to study free surface flow influence on hydrodynamic performance and wake characteristics of flow over hydrofoil. The CFD methodology successfully completed the simulation of breaking and non-breaking flow waves past a hydrofoil beneath free surface.

CHAPTER 5 SIMULATION OF FLOW OVER HYDROPOWER TURBINE

In this chapter, a comprehensive investigation of hydropower turbine performance when it is placed close to free surface is performed, which has never been conducted before. When the turbine is placed close to free surface, a fluid-structure interaction between free surface and the object with complex near-field fluid flow occurs. Understanding this interaction is vital for designing energy harvesting devices. Due to the presence of free surface, turbine may lose some energy to create an unsteady wave in the downstream. Understanding how much energy will lose to create unsteady wave in the downstream is another important objective to investigate. Two sets of validation will be carried out in order to validate the modelling methodology. The numerical results will be presented corresponding to different submerged depths and tip speed ratios (TSR). Lastly, Variable pitch as one of the most common used optimizations for turbine is used to investigate whether or not it is useful to improve the performance of transverse hydropower turbine.

5.1. Mathematical modeling of flow over hydropower turbine

5.1.1. Geometrical characteristics

A vertical axis hydropower turbine with 3 blades of symmetric NACA0018 airfoil section with a chord length (c) of 0.083 m is used for simulation. To facilitate the analysis, a Cartesian coordinate system is used with *x* pointing downstream, and *y* pointing upward. The origin of the coordinate system is located at the center of hydropower turbine. The turbine model consists of three hydrofoils placed at 120 degree each other with two main domains including a stationary domain, and a rotating domain. The rotating subdomain of the turbine is also divided into three independent blade subdomains and the interface boundary condition handles the data exchange between adjacent fields. The boundary conditions between the static and rotating domains are set

to interface to ensure the data exchange. The turbine is submerged in the fluid at the distance h beneath an undisturbed free surface. The computational domain covers an area of $24R \times 16R$ in x and y directions, respectively, and it is split into two zones. Zone I represents air side with dimension of $24R \times 7R$, zone II represents the water zone with the dimension of $24R \times 9R$. The center of turbine stands at $6R$ to the downstream of the inlet. In the downstream of the turbine, $16R$ is reserved for the development of free surface and wake flows.
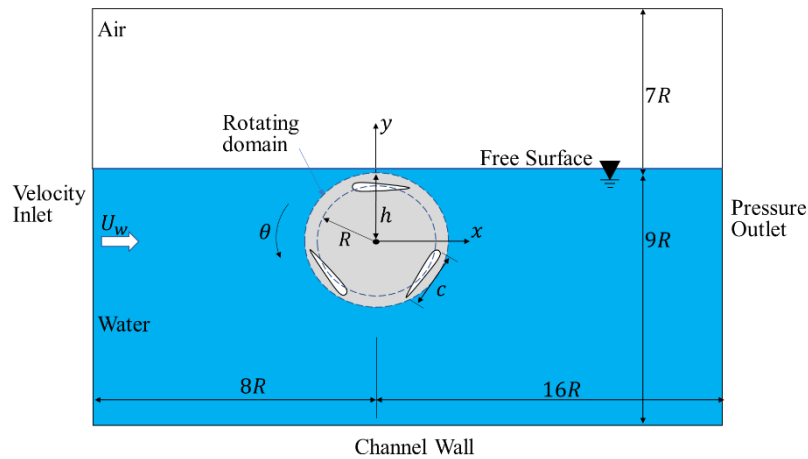
Figure 38. Schematic of flow around hydropower in shallow-tip immersion.

The submerged depth of the turbine is defined as h/R where h is the distance from center of turbine to free surface and R is the radius of the turbine. The flow comes from left side to right side, which involves the two-fluid phases including stationary air as primary fluid and water as secondary fluid entering into the domain with the uniform stream velocity, U_∞, with constant properties including densities (ρ_a for air and ρ_w for water) and the dynamic viscosities (μ_a for air and μ_w for water). Based on the physical description, the main geometrical and operational characteristics of the hydropower turbine are shown in Figure 38 and described in Table 8.

Table 8. Geometrical and operational characteristics of hydropower turbine for current simulation.

Parameter	
Airfoil profile	NACA0018
Chord length, c [m]	0.083
Rotor diameter, D [m]	0.75
Freestream velocity, U_w [m/s]	1
Rotor axis diameter [m]	0.04
Number of blades [-]	3
Moment of inertia of rotor [kg/m^2] (for six DOFs cases)	1.8
Froude numbers based on rotor radius [-]	0.522
Reynolds numbers based on rotor radius [-]	4.1×10^5

5.1.2. Performance parameters

A schematic of the velocity components and force vectors associated with the blade of a hydropower turbine during its rotation is shown in Figure 39. As it is shown in this figure, the free flow velocity is U_w, the rotational speed is ω, the turbine's radius is R, and θ is the blade azimuth angle position. The composition of the turbine rotor peripheral speed $R\omega$ and free flow velocity U_w is the incident velocity of the blade, U_{real}. The velocity components and force vectors constantly change as a function of blade azimuth position which causes a highly variable force loading on the blade and overall rotor. This leads to a fluctuation in power production and cyclical loading.

One of main parameters in design of hydropower turbine is the tip-speed ratio TSR (λ) which is defined as the ratio between the turbine rotor peripheral speed of the turbine rotor and the free flow velocity. The tip-speed ratio can be defined as:

$$TSR = \lambda = \frac{R\omega}{U_\infty}$$

(5.1)

The tip-speed ratio can be calculated as follows:

$$\lambda = sin\theta cot\alpha - cos\theta$$

(5.2)

where α is the blade's angle of attack. The relationship between the azimuthal angle and the blade's angle of attack can be calculated as:

$$\alpha = \arctan\left(\frac{sin\theta}{cos\theta + \lambda}\right) - \varphi \tag{5.3}$$

where φ is the pitch angle of the blade. The hydrodynamics force acting on the blade can be decomposed into the tangential force F_t and normal force F_n which are parallel and perpendicular and parallel to the blade chord, respectively. The tangential force coefficient C_t and the normal force coefficient C_n are represented as (McLaren, 2011):

$$C_t = \frac{F_t}{\frac{1}{2}\rho_w c H U_w^2} \tag{5.4}$$

$$C_n = \frac{F_n}{\frac{1}{2}\rho_w c H U_w^2} \tag{5.5}$$

The torque of a single hydrofoil and the power of the turbine can be calculated as (Zhang et al., 2019):

$$T = \frac{R}{2\pi} \int_0^{2\pi} F_t(\theta)d\theta \tag{5.6}$$

$$P = \frac{R}{2\pi/\omega} \int_0^{2\pi} F_t(\theta)d\theta = N\omega T \tag{5.7}$$

where N is the number of blades on the turbine and $F_t(\theta)$ is the transient tangential force. The hydrodynamic performance of the hydropower turbine can be obtained as:

$$C_T = \frac{c}{2R} \frac{\frac{1}{2\pi}\int_0^{2\pi} F_t(\theta)d\theta}{\frac{1}{2}\rho_w c H U_w^2} \tag{5.8}$$

$$C_P = \frac{N\omega T}{2U_w} \frac{\frac{1}{2\pi}\int_0^{2\pi} F_t(\theta)d\theta}{\frac{1}{2}\rho_w c H U_w^2} \tag{5.9}$$

where H is the height of the rotor, C_T is the torque coefficient, and C_P is the power coefficient.
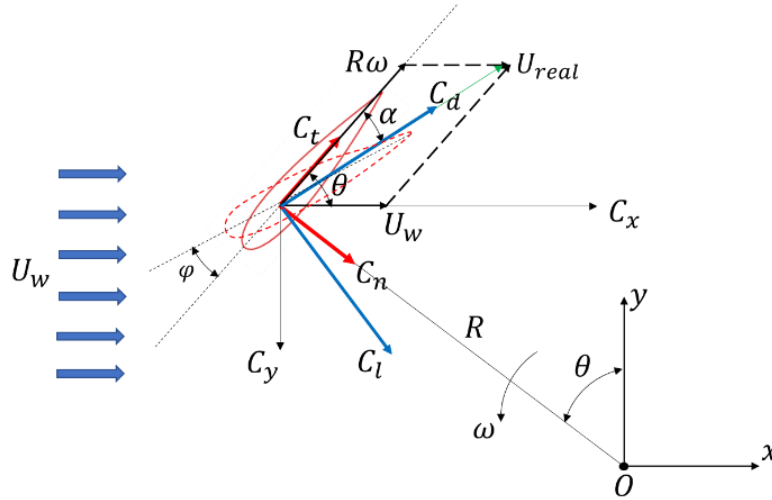
Figure 39. The velocity components and the hydrodynamic force acting on the blade (Zhang et al., 2019).

5.1.3. Grid system of hydropower turbine

In numerical simulation, a high-quality grid system can enhance the efficiency of calculation, the accuracy of solution, and the robustness of convergence. In the process of mesh generation, boundary layer grids close to solid surfaces become more important for complex flow structure. To accurately simulate the flow of the airfoil, refined grids are used in the boundary layer of airfoil. In order to create an appropriate grid system around the boundary layers, y^+ theory is employed. Based on theoretical derivations and experimental explorations, the boundary layers are classified into four parts including viscous sub-layer ($y^+ \leq 5$), buffer layer ($5 < y^+ \leq 30$), log-law region ($30 < y^+ \leq 500$), and outer layer (Versteeg and Malalasekera, 2007). A structured grid system is generated for the computational domain. Figure 40 shows the different regions of the grid system of hydropower turbine. The first mesh close to the solid surface of blade is refined with $y^+ = 1.5$ to ensure that the laminar sub-layer zone is resolved accurately. A growth rate of 1.2 is adopted for all solid surfaces of blades to ensure that

flow structures are accurately captured. The circular rotating inner domain is split into few parts in order to generate a fine structural grid system. To ensure smooth flow continuity through the interface and between the domains of rotors, an equivalent edge sizing on interfaces with a hard enforcing condition is applied in grid system. The mesh system for circular rotating inner domain is also shown in Figure 40a. The rotating domain needs to be created using a fine mesh to capture the wakes around the rotating blades. Figure 40b shows the view of the grid system of whole computational domain, which is relatively fine mesh around the rotating domain and relatively coarse far from the rotating domain. The mesh system in current study contains 533,068 nodes and 529,500 cells. Both validations and all other parts in this work have same mesh system as shown in Figure 40.

(a)   (b)
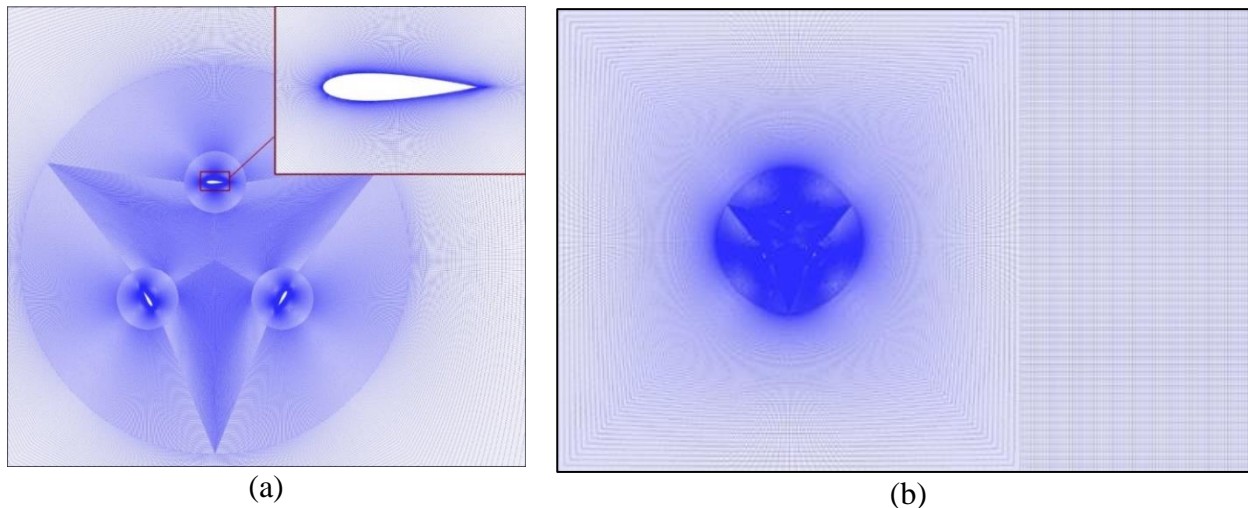
Figure 40. The structural grid system (a) around blade and rotation domain; (b) view of whole computational domain.

5.1.4. Boundary and initial conditions

A velocity inlet is placed on the left side of the computational domain, which has a uniform velocity profile in all cases. The inlet is set as velocity inlet, which has 1 m/s for water

and 0 m/s for air. The outlet boundary is set on the right side of the computational domain as zero relative pressure which represents an open condition on this boundary. Moreover, the solid surface of all blades is set as no-slip boundary condition, and the law of the wall function is applied to the $k - \omega$ turbulence model. Considering the turbulent intensity is unknown at the beginning, a turbulent intensity of 1% and viscosity ratio of 10 are selected for all cases. Bottom side is set as wall in order to simulate the case of shallow water and top is symmetry. The inlet free surface level is set depending on the submerged depths. The interface between rotating inner domain and stationary outer domain is connected by sliding mesh technique. The angular velocities calculated from tip speed ratio (TSR) are added on the cell zone conditions for the first validation and some certain load cases, and six DOFs solver is adapted for the second validation and all other free-to-spin cases. All the cases are initialized by standard mode and absolute value from inlet. The open channel initial condition is set as flat. A transient solver is finally used to predict the turbine's performance over a period of time.

5.2. Flow over a hydropower turbine in vicinity of free surface

The submerged depth of hydropower near free surface could be an integral part of the design and optimization of turbine, and hydrodynamic loadings are expected to be a strong function of the submerged depth. Flow visualization reveals that the interaction of turbine with the free surface is profoundly influenced by the depth of turbine.

Figure 41 shows the effects of submerged depth on the flow structure Instantaneous contours of the water volume fraction at constant tip speed ratio $\lambda = 2$ for different submerged depths h/R=1.2, 1.4, 1.7 and 2 at the last frame of sixth rotation are depicted in this figure. It is observed that the free surface is less disturbed in high submerged depth of h/R=2, however, by decreasing the submerged depth, the wave elevates by the turbine and drops behind it. It is

obvious that the wave break will be less intense with the submerged depth increases. When the submerged depth is small, such as h/R =1.2, 1.4, or 1.7, a wave break can be observed. When the submerged depth become larger, such as h/R =2, a wavy interface between air and water can be observed.

(a)   (b)

(c)   (d)
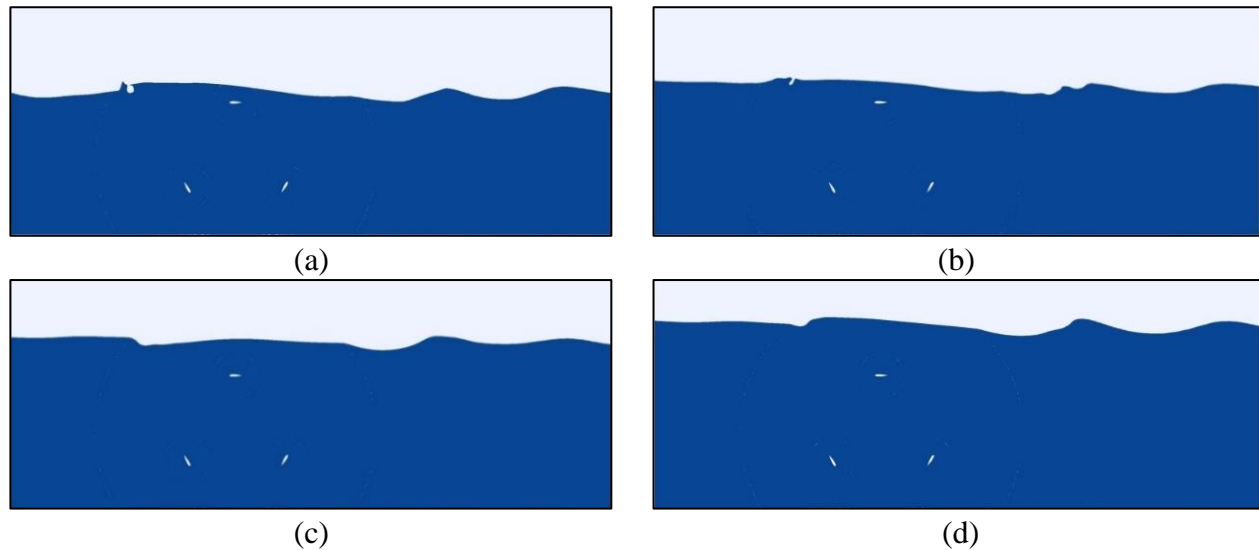
Figure 41. Instantaneous contours of the water volume fraction for tip speed ratio of $\lambda = 2$ at different submerged depths of (a) $h/R = 1.2$; (b) $h/R = 1.4$; (c) $h/R = 1.7$; (d) and $h/R = 2$.

A sequence of frames showing the evolution of flow around the hydropower turbine is shown in Figure 42, which includes the instantaneous contours of the water volume fraction for submergence depths of h/R=1.4 and 1.7 at every 60-degree at tip speed ratio of $\lambda = 2$. In addition, a complete view of wave break can be observed for both cases in this figure.
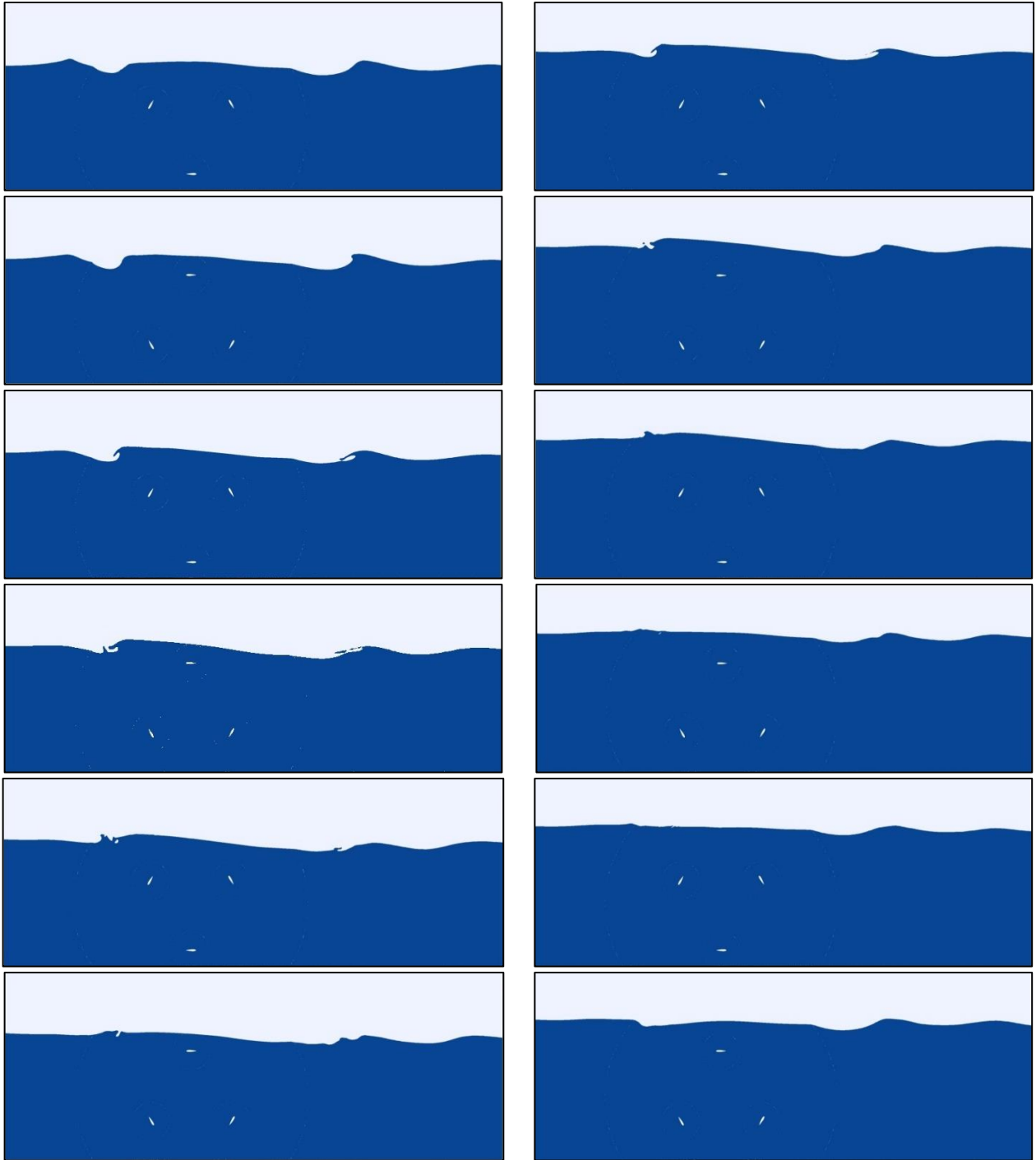
Figure 42. Instantaneous contours of the water volume fraction for tip speed ratio of $\lambda = 2$ at submergence depth (left) h/R=1.4, and (right) h/R=1.7 at every 60-degree.

Figure 43 shows the effects of tip speed ratio on the flow structure, for a constant submerged depth of h/R=1.7. It is clear to see that the surface wave becomes more intense with

the increase of tip speed ratio. In addition, wave break occurs when the tip speed ratio exceeds λ = 2.
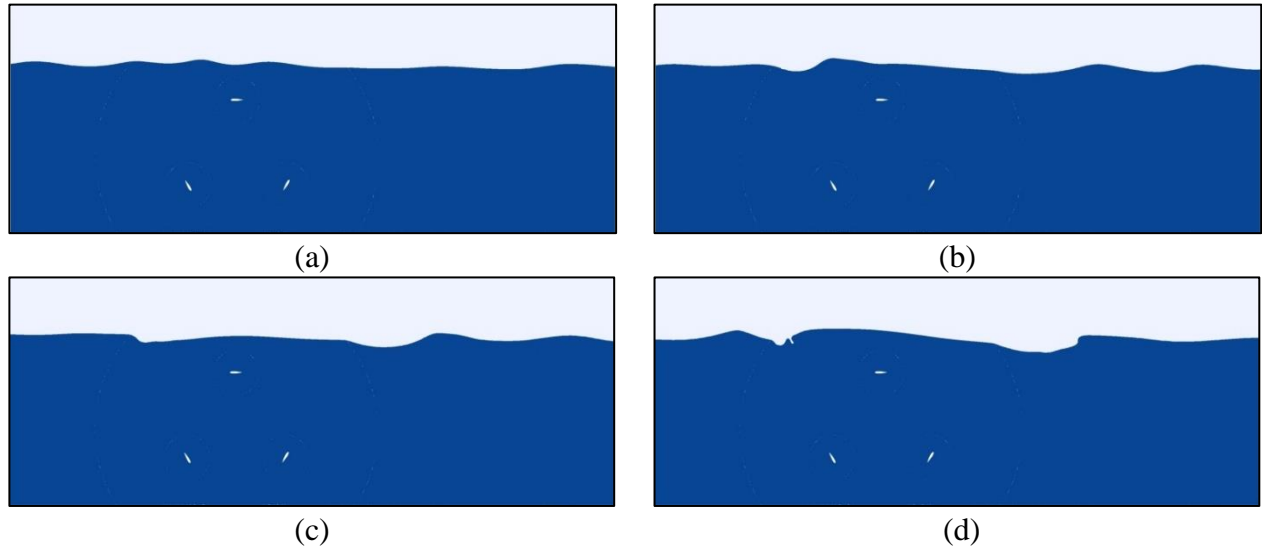
Figure 43. Instantaneous contours of the water volume fraction for submerged depth of h/R=1.7 at different tip speed ratios (a) $\lambda = 1$; (b) $\lambda = 1.5$; (c) $\lambda = 2$; (d) $\lambda = 2.5$.

Figure 44 presents normalized velocity contour of turbine for tip speed ratio $\lambda = 2$ at different submerged depths, which is captured at the middle of sixth rotation. There is a clear low velocity tunnel that can be observed at the wake of hydropower turbine. Also, it is interesting that a jet generated on top of low speed region. The largest free surface elevation occurs for the submerged depth of $h/R = 2$.

Figure 45 shows the normalized velocity profiles in the region near the turbine located at *x*/R=5 for four different submerged depths. The wake velocity at the downstream of the turbine is affected significantly by tip speed ratio. According to this figure, flow accelerates above the center of hydropower turbine due to the limited height of the flow path between the free surface and a low-momentum region. Adding extra rotation to the turbine increases this acceleration, and for the highest TSR, the mean velocity profile shows little evidence of the turbine upstream. A deceleration in fluid flow occurs under the center of turbine in the low-momentum region which

starts growing by adding extra rotation to the turbine which can be understood from flow

visualizations in Figure 44.

(a)
(b)
(c)
(d)
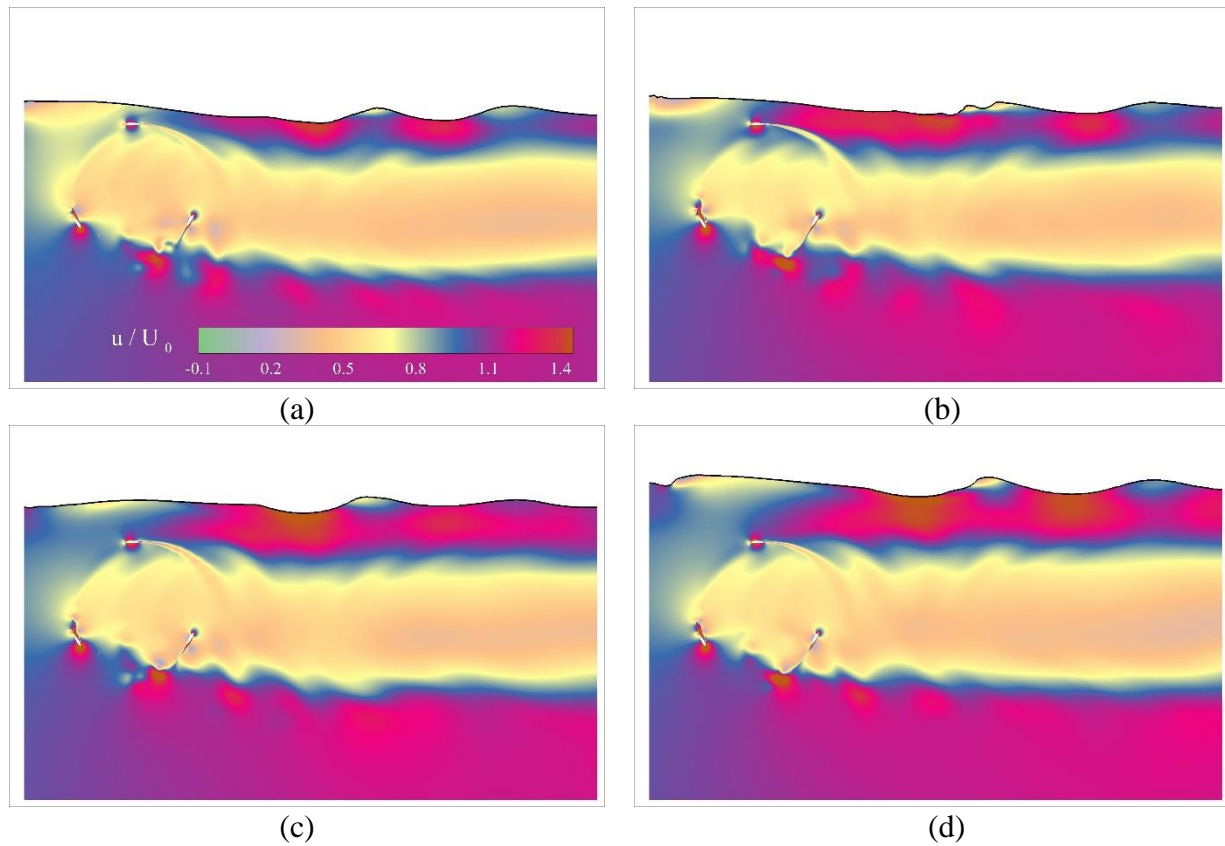
Figure 44. Normalized velocity contour for tip speed ratio $\lambda = 2$ at different submerged depths of (a) $h/R = 1.2$; (b) $h/R = 1.4$; (c) $h/R = 1.7$; (d) and $h/R = 2$.
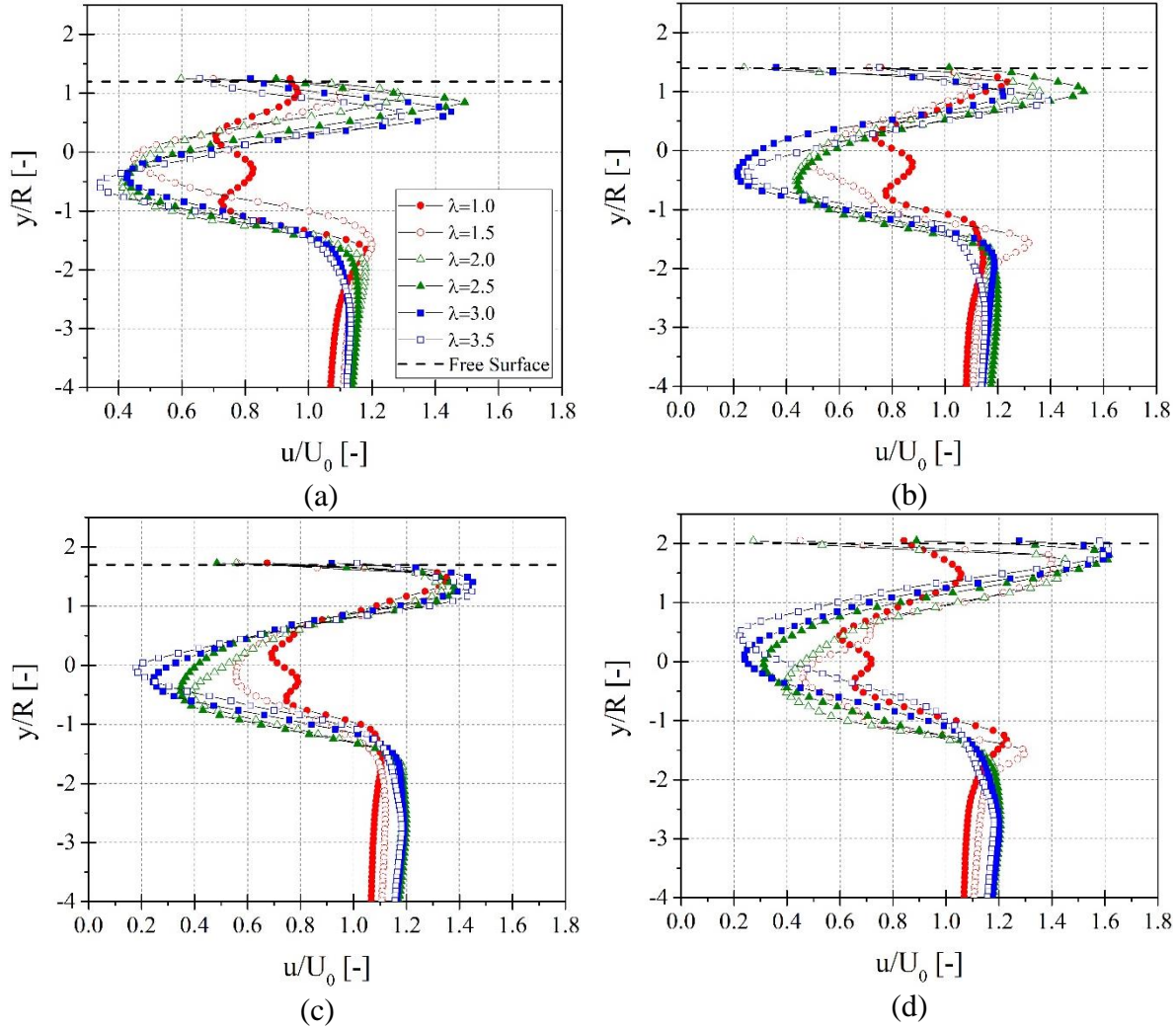
Figure 45. Comparison of the normalized velocity profile at $x/R = 5$ wake structure for various TSR at (a) $h/R = 1.2$; (b) $h/R = 1.4$; (c) $h/R = 1.7$; and (d) $h/R = 2$.

Due to the presence of free surface, a significant difference in the wakes between the high and low TSR can be expected, and it is worth to investigate the effect of submerged depth on the formation and propagation of vortices into the wake. Figure 46 shows the vorticity magnitude for submerged depth of h/R=1.7 and tip speed ratio of $\lambda = 2$. The trace of the shed vortices from the blades on the leeward region traveling downstream is shown in this figure. It can be seen that two pairs of vortices are shed from turbine and then convected behind the turbine within the diameter of turbine. The formation and propagation of vortices is repeated three times per turbine

revolution. The relative distance between the centers of two neighbor vortices are measured and presented in Table 9. The results show that the distance between two neighbor vortices will increase with the decease of submerged depth at small submerged depths, and it basically does not change when the submerged depth over 1.7.
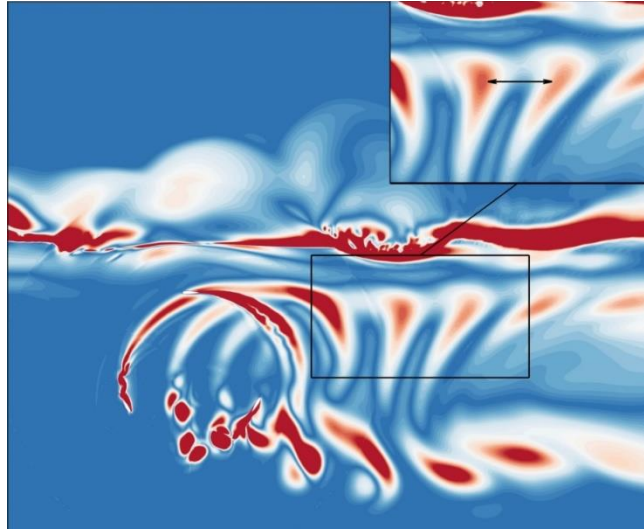
Figure 46. Vorticity magnitude in the near wake of the turbine for submerged depth of h/R =1.7, and tip speed ratio of $\lambda = 2$.

Table 9. The distance between two neighbor vortices.

Submerged depth [-]	Distance [m]
1.2	0.45161
1.4	0.34778
1.7	0.31617
2	0.31778

5.3. Hydrodynamic force characteristics

Figure 47 shows the variations of the normal and tangential coefficients for the hydropower turbine as a function of azimuth angle during rotor rotation at submerged depth of h/R=1.7. The instantaneous normal and tangential coefficients show a periodic change and the cycles within each rotation. A complete harmonic behavior is observed in these coefficients for TSRs more than $\lambda = 2.5$. It also indicates that the peak values of normal and tangential

71

coefficients decrease with the decrease of RSR. This could be due to the presence of free surface and flow becomes smaller with the decrease of TSR. In addition, when the submerged depth decreases, no change occurs at the fluctuation amplitudes of normal and tangential coefficients. The variation of mean normal and tangential coefficients with different tip speed ratios is also shown in Figure 48. The mean tangential coefficient increases with TSR ratio for all submerged depths up to $\lambda = 3$, and then it starts decreasing. A sharp increase is observed for mean normal coefficient between $\lambda = 1.5$ and $\lambda = 3$.
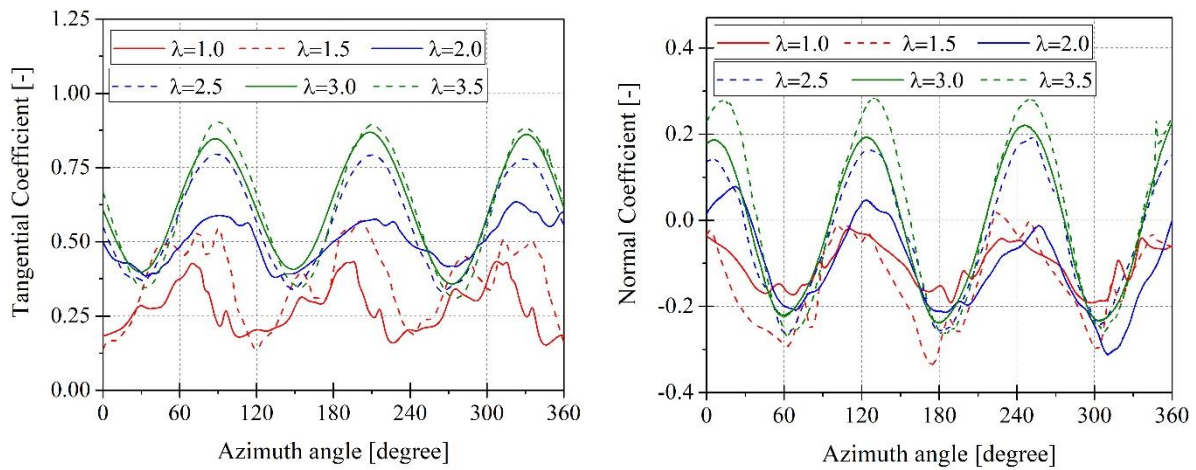
Figure 47. The instantaneous of tangential (left) and normal (right) coefficients for various tip speed ratio at submerged depth $h/R = 1.7$.
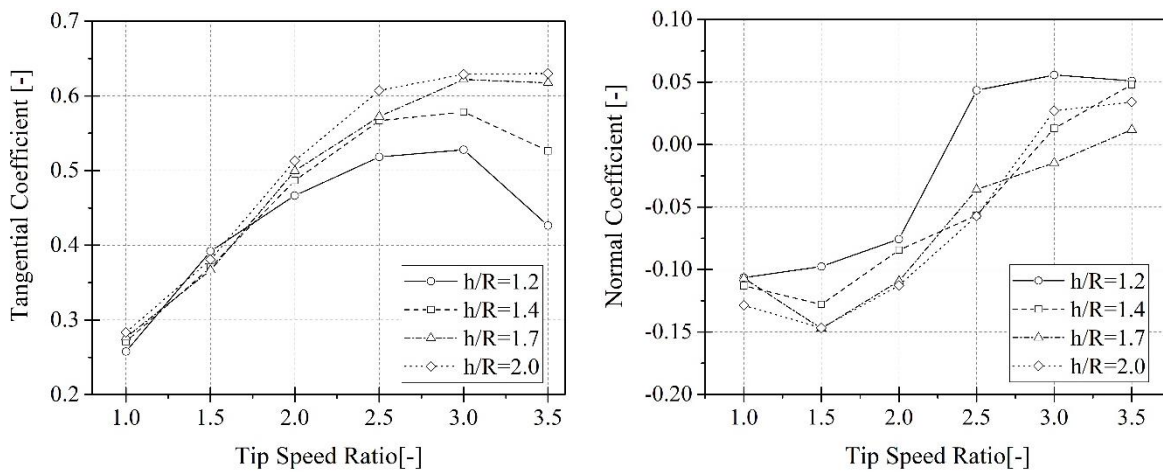
Figure 48. Mean tangential (top) and normal (bottom) coefficient for various tip speed ratio at four different submerged depths.

72

5.4. Torque and power coefficient

Torque coefficient represents how much of torque can a turbine gain from fluid power, which is an important coefficient in all turbine energy devices. Larger torque coefficient means larger power coefficient if tip speed ratio is same. Therefore, improving torque coefficient is an alternative way to increase turbine's efficiency. Additionally, torque coefficient can directly show the power from torque at each significant angular position, which may help improve the power coefficient in a certain degree. Figure 49 shows the torque coefficient versus azimuth angle for four different submerged depths in tip speed ratio of $\lambda = 2$. The maximum torque coefficient for the submerged depth of h/R=2 is equal to about 0.182, while for the submerged depth of h/R=1.2, close to the free surface, the maximum torque coefficient is about 0.0158. It is observed that the peak and average value of torque coefficient drops with the decrease of submerged depth, which results in lower power corresponding to submerged depth.
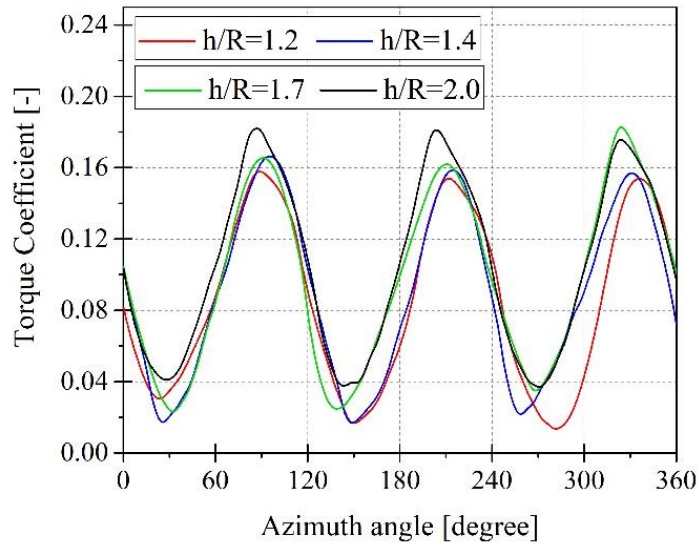
Figure 49. Torque coefficient versus azimuth angle at tip speed ratio of $\lambda = 2$ for various submerged depths.

Figure 50 shows the variation of power coefficient with tip speed ratio for four different submerged depths. The tip speed ratio is altered by changing ω at constant free stream velocity

73

which covers a range of TSR from 1 to 3.5. The analysis of the results reveals that the power

coefficient increases with TSR for all submerged depths and decreases after achieving a

maximum value. The highest power coefficient of 0.25 occurs at a TSR value of 0.25 in

submerged depth of *h*/R=2. It is interesting to note that decreasing the submerged depth from

h/R=2 to *h*/R=1.2 results in about 17% power loss due to the presence of free surface in turbine's

performance.
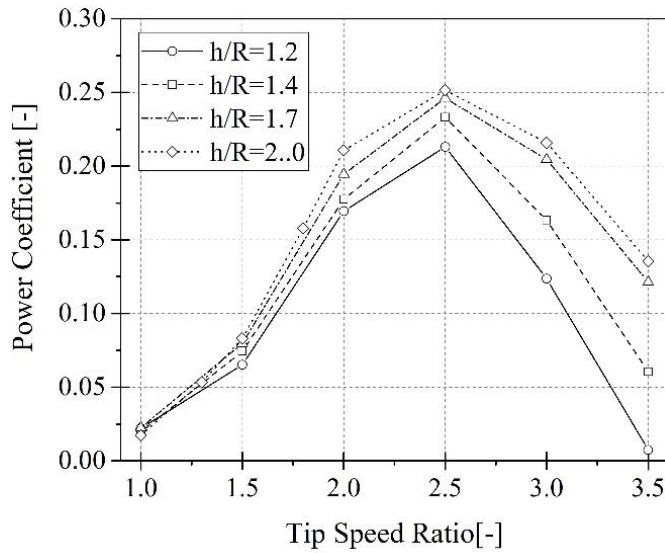
Figure 50. Power coefficient versus tip speed ratio for various submerged depths.

To describe the power coefficient loss due to the presence of free surface, a deep-water

simulation without the presence of free surface is conducted at the optimal tip speed ratio of $\lambda =$

2.5 where the turbine works most optimally. This shows a value of 0.2631 for power coefficient.

The power coefficient loss at optimal tip speed ratio ($\lambda = 2.5$) can be defined as:

$$C_{pl} = C_{p,deep} - C_{pc} \tag{5.10}$$

where C_{pl} is power coefficient loss, $C_{p,deep}$ is power coefficient in deep water and C_{pc} is power

coefficient in specified submerged depth. The power coefficient loss at optimal tip speed ratio

($\lambda = 2.5$) due to submerged depth is shown in Table 10.

Table 10. Power coefficient loss due to the presence of free surface.

Submerged depth, h/R [-]	Power coefficient loss [-]
1.2	0.05012
1.4	0.03005
1.7	0.01695
2	0.01168

5.5. Six DOFs simulations

Numerical prediction is conducted to simulate the hydrokinetic turbine's start-up period.

The six DOFs dynamic method has been adopted and the moment of inertia of all case is set as

I=1.8 kg/m². Tip speed ratio time series during turbine start-up for four different submerged

depths are shown in Figure 51. Apparently, there is no major difference in acceleration period in

all cases while the final steady value rises with the increase of submerged depth.
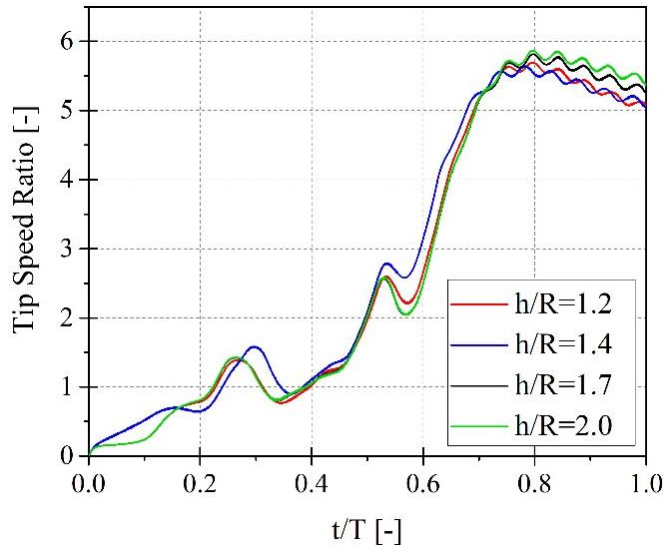
Figure 51. Tip speed ratio time series during turbine start-up for different submerged
depths.

Table 11 presents the steady state tip speed ratio in hydropower turbine for different

submerged depths. As shown in Table 11, considering the effect of free surface in the case of

$h/R = 1.2$ causes a 4.4% difference in angular speed.

Table 11. The steady state tip speed ratio of hydropower turbine.

Submerged depth [-]	Tip speed ratio, λ [-]
1.2	4.7713
1.4	4.8563
1.7	4.9441
2	4.9821

5.6. Blades with variable pitch

Variable pitch optimization method has been becoming widely researched in recent years.

Hwang et al. (2009) adapted a sinusoidal type of variable pitch angles, and claim that there is a

power coefficient improvement of over 25% after adapting the variable pitch. In order to verify

whether the presence of free surface can affect the variable pitch improvement, a set of

numerical simulations is conducted by the same variable pitch method as Hwang et al. (2009).

Figure 52 shows the variable pitch angle varies with the azimuthal angle used in Hwang et al.

(2009) and current study, which is a typical sine wave with 25-degree amplitude.
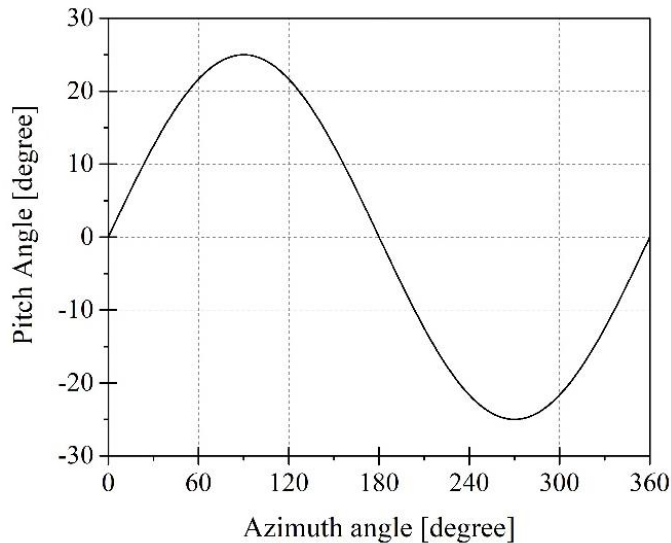
Figure 52. Pitch angle of blade versus azimuthal angles.

The power coefficient corresponding to four submerged depths under the tip speed ratio of $\lambda = 2$ is presented in Table 12. The results reveal that the power coefficient is slightly improved over 25% for submerged depths of $h/R = 1.7$ and $h/R = 2$. However, the power coefficient improvement is relatively small when the hydropower turbine is placed very close to the free surface. Only 1.67% improvement has been found at the case of submerged depth of $h/R = 1.2$.

Table 12. Top tip speed ratio of hydropower turbine in the case of variable pitch.

Submerged depth [-]	Power coefficient [-]	Improvement [%]
1.2	0.1722	1.676
1.4	0.1998	12.59
1.7	0.2461	26.57
2	0.2699	28.09

The low improvement of output power in small submerged depth might be due to this fact that the variable pitch method may increase the free surface intensity, especially in small submerged depth of $h/R = 1.2$, causing wave break with high energy consumption. The comparison of free surface between adapting variable pitch and fixed pitch based on the same tip speed ratio and position is shown in Figure 53. It is clear that the free surface is less disturbed at the submerged depth of $h/R = 2$; however, the free surface has higher intensity and some jets have been created by variable pitch method compared to fixed pitched at the submerged depth of $h/R = 1.2$.
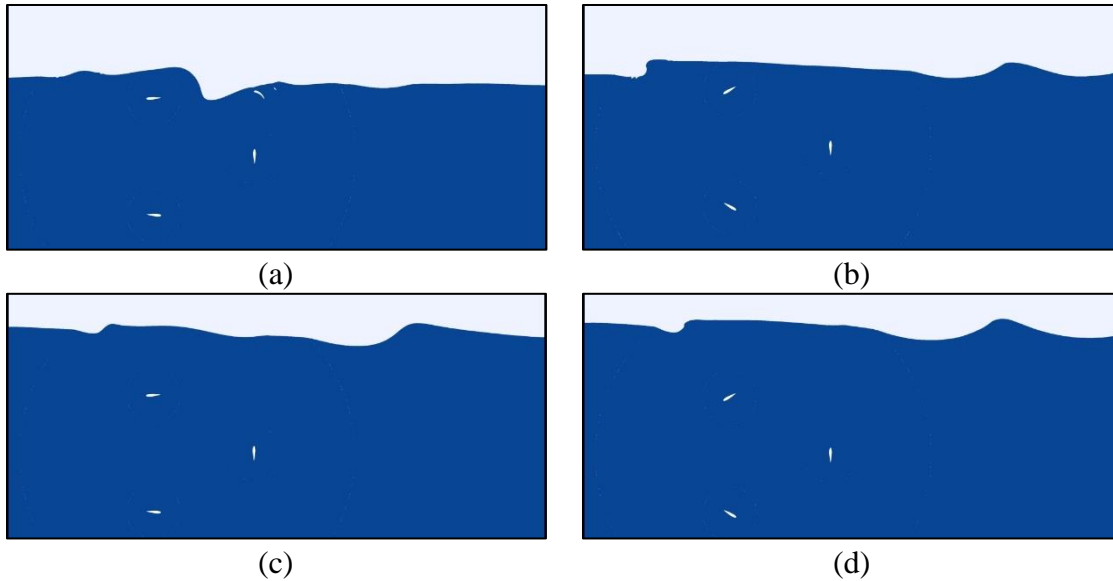
Figure 53. The comparison of free surface between variable pitch (left) and fixed pitch (right) at submerged depths of (a-b) $h/R = 1.2$; and (c-d) $h/R = 2$.

5.7. Summary

Numerical simulations were performed to investigate the fluid-structure interactions between the free surface and hydropower turbine. Varying submerged depths from center of hydropower turbine to free surface for $h/R = 1.2$, 1.4, 1.7, and 2, and tip speed ratio, λ, from 1 to 3.5 were studied for both fixed pitch and variable pitch blades. The multiphase VOF model and SST $k - \omega$ turbulence model were implemented to study the influence of free surface flow on hydrodynamic performance and flow field over hydropower turbine. The wake profile and vorticity magnitude were provided and discussed to investigate the influence of the free surface on turbine's performance. Furthermore, the top speeds for free-to-spin cases were investigated by six DOFs method. Lastly, Variable pitch as one of the most common used optimizations for turbine was used to investigate whether or not it is useful to improve the performance of transverse hydropower turbine.

CHAPTER 6 CONCLUSIONS AND FUTURE WORKS

6.1. Conclusions

In this thesis, the hydrodynamic performance of hydrofoil and hydropower turbine was investigated and discussed under the effect of free surface. Submerged depth as one of the main effective parameters was investigated and discussed in detail. The conclusion of all simulations of flow over single hydrofoil and turbine was discussed respectively as follows.

In chapter 4, the effect of the fluid-structure interactions was investigated for two-dimensional hydrofoil. Varying submerged depths from center of hydrofoil to free surface for $h/c = 0.2, 0.3, 0.5, 0.7$ and 0.9, bulk flow velocities with corresponding Froude numbers (Fr) of 0.1, 0.3, 0.6 and 0.9 , and angles of attack of $\alpha = -15°$ to $+15°$ were studied. The multiphase VOF model and SST $k - \omega$ turbulence model were implemented to study free surface flow influence on hydrodynamic performance and wake characteristics of flow over hydrofoil. It was found that the presence of the free surface can strongly influence hydrofoil performance. The presence of the free surface increased the drag coefficient by 79.01% and reduced the lift coefficient by 33.24% in the case of Froude number of 0.3. Furthermore, the flow velocity also significantly affected the drag and lift coefficients in shallow water. Compared the cases between Froude number of 0.3 and 0.9, high flow velocity reduced the drag coefficient by 79.01% the lift coefficient by 93.53% in the case of submerged depth of $h/c = 0.3$ and angle of attack of $\alpha = +5°$. It was also found that the presence of hydrofoil can affect the free surface shape both in upstream and downstream. The surface wave break occurred when hydrofoil was very close to the free surface, and free surface showed sinusoidal wave in downstream when hydrofoil was not very close to the free surface. There is no wave breaking occurring at submerged depth of $h/c = 0.9$ in this larger scheme simulation. Therefore, it is obvious to get an assumption that the

breaking condition was not only related to relative submerged depth, h/c, but also depended on the absolute submergence height, h.

In chapter 5, numerical simulations were performed to investigate the fluid-structure interactions between the free surface and hydropower turbine. Varying submerged depths from center of hydropower turbine to free surface for $h/R = 1.2$, 1.4, 1.7, and 2, and tip speed ratio, λ, from 1 to 3.5 were studied for both fixed pitch and variable pitch blades. The multiphase VOF model and SST $k - \omega$ turbulence model were implemented to study the influence of free surface flow on hydrodynamic performance and flow field over hydropower turbine. It was found that the presence of the free surface decreased the power coefficient by 19.05% for the closest submerged depth studied at the optimal tip speed ratio. The power coefficient decreased more with smaller submerged depth at higher tip speed ratio. Furthermore, the wave breaking was observed when the submerged depth h/R was smaller than 2. The free surface became more unsteady with the increase of the tip speed ratio, which was probably the reason that more power loss occurred with the increase of tip speed ratio. Moreover, the wake profile and vorticity magnitude were provided and discussed to investigate the influence of the free surface on turbine's performance. It was found that the distance between two neighbor vortices was increased with the decease of submerged depth at small submerged depths, and no change was observed when the submerged depth was over $h/R = 1.7$. Lastly, Variable pitch effectively improved the power coefficient by 28.10% when the free surface was far from the hydropower turbine, which was close to the results from previous researches without free surface. However, the power coefficient improvement became significantly small when the hydropower turbine was located very close to the free surface.

6.2. Future works

As future works, a list of possible extra works can be performed to improve the current study:

- The effect of airfoil shape on hydrodynamic characteristics can be investigated in both single hydrofoil and turbine cases.

- A 3D simulation of flow over hydropower turbine can be performed to observe the effect of 3D simplification on the performance of the turbine.

- The effect of number of blades on performance can be studied by adding more than blades to the hydropower turbine.

- Other turbulence models such as Detached eddy simulation (DES) and Large Eddy Simulation (LES) models can be used in both single hydrofoil and turbine simulations to capture all eddies in the flow.

- More feasible variable pitch motion, such as variable pitch with flux line theory, with the presence of free surface is also a good topic.

REFERENCES

ANSYS FLUENT User Guide Release 19.1, 2018.

Aparna, D., Ramadan, R., 2017. CFD Analysis of Tidal Turbine Blades. Proceeding of the 2017 IEEE Region 10 Conference (TENCON), Malaysia, November 5-8.

Asr, M.T., Nezhad, E.Z., Mustapha, F., Wiriadidjaja, S., 2016. Study on start-up characteristics of H-Darrieus vertical axis wind turbines comprising NACA 4-digit series blade airfoil. Energy 112; 528-537.

Babarit, A., 2017. Ocean wave energy conversion: resource, technologies and performance. Elsevier Nov 17.

Bianchini, A., Carnevale, E., and Ferrari, L., 2011. A model to account for the virtual camber effect in the performance prediction of an H-Darrieus VAWT using the momentum models. Wind Engineering 35(4); 465-482.

Birjandi, A. H., Bibeau, E. L., Chatoorgoon V., Kumar, A., 2013. Power measurement of hydrokinetic turbines with free-surface and blockage effect. Ocean Engineering 69; 9-17.

Blenkinsopp, C.E., Chaplin, J.R., 2008. The effect of relative crest submergence on wave breaking over submerged slopes. Coastal Engineering 55; 967–974.

Borg, M., Shires, A., Collu, M., 2014. Offshore floating vertical axis wind turbines, dynamics modelling state of the art. Part I: Aerodynamics. Renewable and Sustainable Energy Reviews 39; 1214-1225.

Bose, S.R., Chandramouli, S., Premsai, T.P., Prithviraj, P., Vivek, M., Velamati, R.K., 2014. Numerical Analysis of Effect of Pitch Angle on a Small Scale Vertical Axis Wind Turbine. International Journal of Renewable Energy Research 4(4); 929-935.

Bouscasse, B., Colagrossi, A., Marronea, S., Souto-Iglesias, A., 2017. SPH modelling of viscous flow past a circular cylinder interacting with a free surface. Computers and Fluids 146; 190-212.

Bubbar, K., 2018, Conceptual design of wave energy converters. PhD diss., University of Victoria.

Budal, K., Falnes, J., 1975. A resonant point absorber of ocean-wave power. Nature 256; 478-479.

Chapman, J., Gross, R., 2001. Technical and economic potential of renewable energy generating technologies: Potentials and cost reductions to 2020. Foresight Energies from Sea-Towards, 2001, pp. 2020.

Chua, K., 2002. Design and testing of a vertical axis wind turbine rotor. BEng Project Report, Faculty of Mechanical Engineering, University of Technology, Malaysia.

Day, A.H., Babarit, A., Fontaine, A., He, Y.P., Kraskowski, M., Murai, M., Penesis, I., Salvatore, F., Shin, H.K., 2015. Hydrodynamic modelling of marine renewable energy devices: A state of the art review. Ocean Engineering 108; 46-69.

Duncan, J. H., 1981. An experimental investigation of breaking waves produced by a towed hydrofoil. Proc. R. SOC. Lond. A 377; 331-348.

Duncan, J. H., 1983. The breaking and non-breaking wave resistance of a two-dimensional hydrofoil. Journal of Fluid Mechanics 126; 507-520.

Evans, D.V., 1976. A theory for wave-power absorption by oscillating bodies. Journal of Fluid Mechanics 77, 1–25.

Ferreira, C. S., van Bussel, G., van Kuik, G., 2007. 2D CFD simulation of dynamic stall on a vertical axis wind turbine: verification and validation with PIV measurements. In: 45th AIAA aerospace sciences meeting and exhibit. Nevada, Reno.

Filianoti, P., Gurnari, L., Torresi, M., Camporeale., 2018. CFD analysis of the energy conversion process in a fixed oscillating water column (OWC) device with a Wells turbine. 73rd Conference of the Italian Thermal Machines Engineering Association (ATI 2018) 12-14 September, Pisa Italy.

Filippas, E.S., Belibassakis, K.A., 2014. Hydrodynamic analysis of flapping-foil thrusters operating beneath the free surface and in waves. Engineering Analysis with Boundary Elements 41; 47-59.

Hill, N., Dominy, R., Ingram, G., and Dominy, J., 2009. Darrieus turbines: the physics of self-starting. Proceedings of the Institution of Mechanical Engineers Part A: Journal of Power and Energy 223(1); 21-29.

Hino, T., Martinelli, L., Jameson, A., 1993. A finite-volume method with unstructured grid for free surface flow simulations. In 6th International conference on numerical ship hydrodynamics.

Hirt, C. W., Nichols, B. D., 1981. Volume of fluid (vof) method for the dynamics of free boundaries. Journal of Computational Physics, 39; 201-225.

Hough, G.R., Moran, S.P., 1969. Froude number effects on two-dimensional hydrofoils. Journal of Ship Research 13; 53-60.

Hwang, I.S., Lee, Y.H., Kim, S.J., 2009. Optimization of cycloidal water turbine and the performance improvement by individual blade control. Applied Energy 86; 1532-1540.

Ikoma, T., Eto, H., Masuda, K., Rheem, C. K., 2018. Turbine Performance of Pitch-Contolled VAMTs from Flume Tests and a Sea Test. OCEANS-MTS/IEEE Kobe Techno-Oceans (OTO) (pp. 1-6). IEEE.

Kaniecki, M., Krzemianowski, Z., 2016. CFD based analysis of silt erosion in Kaplan hydraulic turbine. International Conference on Signal Processing, Communication, Power and Embedded System (SCOPES) (pp. 1765-1770). IEEE.

Karim, M. M., Prasad, B., Rahman, N., 2014. Numerical simulation of free surface water wave for the flow around NACA 0015 hydrofoil using the volume of fluid (VOF) method. Ocean Engineering 78; 89-94.

Kennell, C., Plotkin, A., 1984. A second order theory for the potential flow about thin hydrofoils. Journal of Ship Research 28; 55-64.

Le, T.Q., Lee, K.S., Park, J.S., Ko, J.H., 2014. Flow-driven rotor simulation of vertical axis tidal turbines: A comparison of helical and straight blades. International Journal of Naval Architecture and Ocean Engineering 6(2); 257-268.

Liu, I.H., Riglin, J., Schleicher, W.C., Oztekin, A., 2016. Flow past a plate in the vicinity of a free surface. Ocean Engineering 111; 323-334.

Longuet-Hihhins, M.S., 1982. Parametric solutions for breaking waves. Journal of Fluid Mechanics 121; 403-424.

Malavasi, S., Guadagnini, A., 2007. Interactions between a rectangular cylinder and a free-surface flow. Journal of Fluids and Structures 23(8); 1137-1148.

McLaren, K.W., 2011. A Numerical and Experimental Study of Unsteady Loading of High Solidity Vertical axis Wind Turbines, McMaster University.

Menter, F.R., 1993. Zonal Two Equation k-turbulence Models for Aerodynamic Flows. AIAA Paper 2906.

Menter, F.R., 1994. Two-equation eddy-viscosity turbulence models for engineering applications. AIAA Journal 32(8); 1598-1605.

Menter, F.R., Kuntz, M., Langtry, R., 2003. Ten years of industrial experience with the SST turbulence model. Turbulence Heat and Mass Transfer 4; 625-632.

Mertens, S., 2006. Wind energy in the built environment: concentrator effects of buildings. TU Delft: Delft University of Technology.

Miyata, H., Shikazono, N., Kanai, M., 1990. Forces on a circular cylinder advancing steadily beneath the free-surface. Ocean Engineering 17(1–2); 81–104.

Muljadi, E., Yu, Y., 2015. Review of Marine Hydrokinetic Power Generation and Power Plant. Electric Power Components and Systems 43(12); 1422-1433.

Office of energy efficiency and renewable energy. History of U.S. Wind Energy. Available at: https://www.energy.gov/eere/wind/wind-energy-basics

Ohm, A., Tetursson, H., 2017. Automated CFD Optimization of a Small Hydro Turbine for Water Distribution Networks. Chalmers University of Technology: Göteborg, Sweden.

Parkin, B.R., Perry, B., Wu, T.Y., 1956. Pressure distribution on a hydrofoil running near the water surface. Journal of Applied Physics 27; 232-240.

Prasad, B., Hino, T., Suzuki, K., 2015. Numerical simulation of free surface flows around shallowly submerged hydrofoil by OpenFOAM. Ocean Engineering 102; 87-94.

Rainbird, J.M., 2007. The aerodynamic development of a vertical axis wind turbine. MEng Project Report, School of Engineering, University of Durham, UK.

Rainbird, J.M., 2016. Blockage tolerant wind tunnel testing of aerofoils at angles of incidence from 0◦ to 360◦, with respect to the self-start of vertical-axis wind turbines, PhD Thesis, Imperial College London, UK.

Reichl, P., Houriganand, K., Thompson, M., 2005. Flow past a cylinder close to a free surface. Journal of Fluid Mechanics 533; 269-296.

Riglin, J., Schleicher, W. C., Liu, I. H., Oztekin, A. 2015. Characterization of a micro-hydrokinetic turbine in close proximity to the free surface. Ocean Engineering 110; 270-280.

Siegel, S., 2019. Numerical benchmarking study of a cycloidal wave energy converter. Renewable Energy 134; 390-405.

Sangal, S., Singhal, M. K., Saini, R.P., 2016. CFD based analysis of silt erosion in Kaplan hydraulic turbine. International Conference on Signal Processing, Communication, Power and Embedded System (SCOPES) (pp. 1765-1770). IEEE.

Sheridan, J., Lin, J.C., Rockwell, D., 1997. Flow past a cylinder close to a free surface. Journal of Fluid Mechanics. 330; 1-30.

Subramanian, A., Yogesh, S.A., Sivanandan, H., Giri, A., Vasudevan, M., Mugundhan, V., Velamati, R.K., 2017. Effect of airfoil and solidity on performance of small scale vertical axis wind turbine using three dimensional CFD model. Energy 133(15); 179-190.

Suzuki, Y., Katayama, Y., Watanabe, S., Tsuda, S., Furukawa, A., 2019. A study on performance prediction of Darrieus-type hydroturbine operated in open channels using CFD with

actuator disk method. In IOP Conference Series: Earth and Environmental Science (Vol. 240, No. 4, p. 042020).

Teran, L. A., Larrahondo, F. J., Rodríguez, S. A., 2016. Performance improvement of a 500-kW Francis turbine based on CFD. Renewable energy, 96; 977-992.

U.S. Energy Information Administration, 2016. Wind and Solar Data and Projections from the U.S. Energy Information Administration: Past Performance and Ongoing Enhancements. Available from: https://www.eia.gov/outlooks/aeo/supplement/renewable/pdf/projections.pdf

U.S. Energy Information Administration, April 2019, Monthly Energy. Available from: https://www.eia.gov/totalenergy/data/monthly/archive/00351904.pdf

Versteeg, H.K., Malalasekera, W., 2007. An Introduction to Computational Fluid Dynamics, Pearson Education Limited, England, UK, ISBN 978-0-13- 127498-3.

Wang, J. F., Piechna, J., Müller, N., 2012. A novel design of composite water turbine using CFD. Journal of Hydrodynamics, Ser. B 24(1); 11-16.

Whelan, J. I., Graham, J.M.R., Peiro, J., 2009. A free-surface and blockage correction for tidal turbines. Journal of Fluid Mechanics 624; 281-291.

Wilcox, D., 1993. Turbulence modeling for CFD. DCW Industries, Inc. CA.

Wu, T.R., Chu, C.R., Huang, C. J., Wang, C.Y., Chien, S. Y., Chen, M. Z., 2014. A two-way coupled simulation of moving solids in freesurface flows. Computer and Fluid 100; 347-355.

Xie, N. and Vassalos, D., 2007. Performance analysis of 3D hydrofoil under free surface. Ocean Engineering 34; 1257-1264.

Zhang, T., Elsakka, M., Huang, W., Wang, Z., Ingham, D.B., Ma, L., Pourkashanian, M., 2019. Winglet design for vertical axis wind turbines based on a design of experiment and CFD approach. Energy Conversion and Management 195; 712-726.

APPENDIX A:

INSITITUTIONAL REVIEW BOARD LETTER

MARSHALL UNIVERSITY.
www.marshall.edu

Office of Research Integrity

December 6, 2019

Zeda Yin
1510 7th Avenue, Apt. 4
Huntington, WV 25701

Dear Mr. Yin:

This letter is in response to the submitted thesis abstract entitled *"Numerical Simulation for the Hydrodynamic Performance of Hydropower Turbine Near Free Surface."* After assessing the abstract, it has been deemed not to be human subject research and therefore exempt from oversight of the Marshall University Institutional Review Board (IRB). The Code of Federal Regulations (45CFR46) has set forth the criteria utilized in making this determination. Since the information in this study does not involve human subjects as defined in the above referenced instruction, it is not considered human subject research. If there are any changes to the abstract you provided then you would need to resubmit that information to the Office of Research Integrity for review and a determination.

I appreciate your willingness to submit the abstract for determination. Please feel free to contact the Office of Research Integrity if you have any questions regarding future protocols that may require IRB review.

Sincerely,

Bruce F. Day, ThD, CIP
Director

WE ARE... MARSHALL.
One John Marshall Drive • Huntington, West Virginia 25755 • Tel 304/696-4303
A State University of West Virginia • An Affirmative Action/Equal Opportunity Employer

87

APPENDIX B:

NOMENCLATURE

c Blade chord [m]

C_D Drag coefficient [-]

C_L Lift coefficient [-]

C_n Normal force coefficient [-]

C_P Power Coefficient [-]

C_t Tangential force coefficient [-]

C_T Torque coefficient [-]

D   Rotor diameter [m]

d   Cylinder diameter [m]

F_D Drag Force [N]

F_L Lift Force [N]

F_n Normal Force [N]

Fr Froude number [-]

F_t Tangential Force [N]

H Characteristic depth [m]

N Number of blades [-]

P Power [W]

R   Turbine radius [m]

Re Reynolds number [-]

U_∞ Freestream velocity [m/s]

Greek

α Angle of attack [degree]

θ Azimuthal angle [degree]

φ Blade pitch angle [degree]

λ Tip speed ratio [-]

ρ_a Density of air [kg/m^3]

ρ_w Density of water [kg/m^3]

ω Rotational velocity [rad/s]

μ_a Dynamic viscosity of air [Pa s]

μ_w Dynamic viscosity of water [Pa s]

u_τ Friction velocity [m/s]

Subscripts/Superscripts

D Drag

L   Lift

n Normal

P Power

t Tangential

∞   Freestream

APPENDIX C:

THE UDF CODE FOR VARIABLE PITCH CASE

```
#include "udf.h"

# define PI 3.14159265

# define r 0.375

DEFINE_TRANSIENT_PROFILE(speed_1,time_1)

{

real amp_1 = PI/52.2512*45;

real freq_1 = 5.333333333;

real omega_1;

omega_1 = -amp_1 * cos(freq_1 * time_1);

return omega_1;

}

/***define angular velocity for blade 1***/

DEFINE_TRANSIENT_PROFILE(speed_2,time_2)

{

real amp_2 = PI/52.2512*45;

real freq_2 = 5.333333333;

real omega_2;

omega_2 = amp_2 * cos(freq_2 * (time_2 + 2*PI/3));

return omega_2;

}

/***define angular velocity for blade 2***/
```

```
DEFINE_TRANSIENT_PROFILE(speed_3,time_3)

{

real amp_3 = PI/52.2512*45;

real freq_3 = 5.333333333;

real omega_3;

omega_3 = amp_3 * cos(freq_3 * (time_3 - 2*PI/3));

return omega_3;

}

/***define angular velocity for blade 3***/

DEFINE_TRANSIENT_PROFILE(po_x1,time_1)

{

real position_x1;

position_x1 = - r * sin(2*PI/0.1780973*time_1);

return position_x1;

}

/***define x axis position for blade 1***/

DEFINE_TRANSIENT_PROFILE(po_y1,time_1)

{

real position_y1;

position_y1 = r * cos(2*PI/0.1780973*time_1);

return position_y1;

}
```

```
/***define y axis position for blade 1***/

DEFINE_TRANSIENT_PROFILE(po_x2,time_2)

{

real position_x2;

position_x2 = -r * sin(2*PI/0.1780973* (time_2 + 2*PI/3));

return position_x2;

}

/***define x axis position for blade 2***/

DEFINE_TRANSIENT_PROFILE(po_y2,time_2)

{

real position_y2;

position_y2 = r * cos(2*PI/0.1780973* (time_2 + 2*PI/3));

return position_y2;

}

/***define y axis position for blade 2***/

DEFINE_TRANSIENT_PROFILE(po_x3,time_3)

{

real position_x3;

position_x3 = -r * sin(2*PI/0.1780973* (time_3 - 2*PI/3));

return position_x3;

}

/***define x axis position for blade 3***/

DEFINE_TRANSIENT_PROFILE(po_y3,time_3)
```

```
    {

    real position_y3;

    position_y3 = r* cos(2*PI/0.1780973* (time_3 - 2*PI/3));

    return position_y3;

}

    /***define y axis position for blade 3***/
```